

# The Formation of Pluto's Low Mass Satellites

Scott J. Kenyon

*Smithsonian Astrophysical Observatory, 60 Garden Street, Cambridge, MA 02138*

e-mail: skenyon@cfa.harvard.edu

Benjamin C. Bromley

*Department of Physics, University of Utah, 201 JFB, Salt Lake City, UT 84112*

e-mail: bromley@physics.utah.edu

## ABSTRACT

Motivated by the *New Horizons* mission, we consider how Pluto's small satellites – currently P5, Nix, P4, and Hydra – grow in debris from the giant impact that forms the Pluto–Charon binary or in solid material captured from the protoplanetary debris disk. If the satellites have masses close to their minimum masses, our analysis suggests that capture of material into a circumplanetary or circumbinary debris disk is a viable mechanism for satellite formation. If the satellites are more massive, they probably form in debris from the giant impact. After the impact, Pluto and Charon accrete some of the debris and eject the rest from the binary orbit. During the ejection, high velocity collisions among debris particles produce a collisional cascade, leading to the ejection of some debris from the system and enabling the remaining debris particles to find stable orbits around the binary. Our numerical simulations of viscous diffusion, coagulation, and migration show that collisional evolution within a ring or disk of debris leads to a few small satellites orbiting Pluto–Charon. These simulations are the first to demonstrate migration-induced mergers within a particle disk. The final satellite masses correlate with the initial disk mass. More massive disks tend to produce fewer satellites. For the current properties of the satellites, our results strongly favor initial debris masses of  $3 - 10 \times 10^{19}$  g and current satellite albedos  $A \approx 0.4-1$ . We also predict an ensemble of smaller satellites,  $R \lesssim 1-3$  km, and very small particles,  $R \approx 1-100$  cm and optical depth  $\tau \lesssim 10^{-10}$ . These objects should have semimajor axes outside the current orbit of Hydra.

*Subject headings:* Planetary systems – Planets and satellites: formation – Planets and satellites: physical evolution – Kuiper belt: general

## 1. INTRODUCTION

The Pluto–Charon binary is an icy jewel of the solar system. Discovered in 1978 (Christy & Harrington 1978; Noll et al. 2008, and references therein), the central binary has a mass ratio,  $q_{PC} \equiv M_C / (M_P + M_C) = 0.10$  (where  $M_P \approx 1.3 \times 10^{25}$  g is the mass of Pluto and  $M_C \approx 1.5 \times 10^{24}$  g is the mass of Charon; Buie et al. 2006), an orbital semimajor axis  $a_{PC} \approx 17 R_P$  (Pluto radii;  $1 R_P \approx 1160$  km; Young & Binzel 1994; Young et al. 2007), and an orbital period  $T_{PC} \approx 6.4$  d (e.g., Sicardy et al. 2006; Buie et al. 2006). Four satellites – P5, Nix, P4, and Hydra – orbit at semimajor axes,  $a_{P5} \approx 39 R_P$ ,  $a_{Nix} \approx 43 R_P$ ,  $a_{P4} \approx 49 R_P$ , and  $a_{Hydra} \approx 57 R_P$  (Weaver et al. 2006; Showalter et al. 2011, 2012). Curiously, the orbital periods of the satellites are roughly 3 (P5), 4 (Nix), 5 (P4), and 6 (Hydra) times the orbital period of Charon. Although the satellite masses are uncertain by at least an order of magnitude (e.g., Buie et al. 2006; Tholen et al. 2008), they are much smaller than the mass of the Pluto–Charon binary. For an albedo  $A$  and a mass density  $\rho = 1$  g cm<sup>-3</sup>, the masses are  $M_{P5} \approx 9 \times 10^{16} A^{-3/2}$  g,  $M_N \approx 8.4 \times 10^{18} A^{-3/2}$  g,  $M_{P4} \approx 2.6 \times 10^{17} A^{-3/2}$  g, and  $M_H \approx 1.4 \times 10^{19} A^{-3/2}$  g (e.g., Buie et al. 2006; Showalter et al. 2011; Youdin et al. 2012; Showalter et al. 2012). For  $A \approx 0.04$ – $1$  (e.g., Marcialis et al. 1992; Roush et al. 1996; Stansberry et al. 2008; Brucker et al. 2009), the combined mass of the four small satellites is  $M_s \approx 3$ – $300 \times 10^{19}$  g  $\approx 2.3$ – $230 \times 10^{-6} M_P$ .

The architecture of Pluto–Charon and the four smaller satellites provides fascinating tests for the dynamical stability of multiple systems (e.g., Lee & Peale 2006; Tholen et al. 2008; Süli & Zsigmond 2009; Winter et al. 2010; Peale et al. 2011; Youdin et al. 2012). Dynamical fits of orbits to observations yield constraints on the masses, radii, and albedos of the satellites. Analyses using the restricted three body problem or  $n$ -body simulations identify stable orbits surrounding Pluto–Charon and place additional constraints on the masses of the satellites. Taken together, current theoretical results for Nix, P4, and Hydra suggest masses (albedos) close to the lower (upper) limits derived from dynamical fits to observations, with  $M_s \lesssim 2.5 \times 10^{20}$  g and  $A \gtrsim 0.2$  (Youdin et al. 2012).

The system also challenges planet formation theories. Currently, most ideas center on a giant impact scenario, where the Pluto–Charon binary forms during a collision between two icy objects with masses  $M_1 \approx M_P$  and  $M_2 \approx (1 - q)q^{-1}M_P$ , where  $q \approx 0.25$ – $0.33$  (McKinnon 1989; Canup 2005, 2011). Immediately after the impact, the binary has an initial separation of 5–10  $R_P$ . Over 1–10 Myr, tidal evolution synchronizes the rotation of Pluto–Charon and then circularizes and expands the binary to its present separation (Farinella et al. 1979; Dobrovolskis et al. 1997).

In some scenarios, the small satellites also form during the giant impact (e.g., Stern et al. 2006; Canup 2011). Prior to the discovery of P4/P5, Ward & Canup (2006) developed an

elegant model where the satellites move outward during the expansion of the Pluto–Charon orbit. If the Pluto–Charon orbit is eccentric throughout the expansion, resonant interactions with Charon can maintain the 1:4:6 period ratio of Charon, Nix, and Hydra. Ward & Canup (2006) comment that a lower mass satellite might orbit with a 5:1 period ratio. However, they also note that most of the impact debris probably developed high eccentricity orbits. High velocity collisions of debris particles complicate the ability of Charon to maintain a 3:4:5:6 period ratio for four satellites.

Lithwick & Wu (2008) consider another path for satellite formation. Their analytic and numerical calculations suggest that maintaining the 4:1 (Nix) and 6:1 (Hydra) period ratios in an expanding binary requires mutually exclusive eccentricity evolution for the Pluto–Charon binary (see also Peale et al. 2011). Tidal interactions between Nix and Charon might establish the 4:1 period ratio, while interactions between Nix and Hydra establish the 4:6 period ratio. However, they consider this possibility unlikely. Instead, they propose that the Pluto–Charon binary captured many small planetesimals into a disk. Collisional evolution then led to the formation of P5, Nix, P4, and Hydra; orbital migration later drove the orbits into their current configuration.

Here, we consider whether the Pluto–Charon small satellites grow approximately *in situ* from material ejected during the impact or captured from the solar debris disk. We begin by demonstrating that a giant impact capable of forming Pluto–Charon is a natural outcome of scenarios for planet formation at 15–40 AU. After the impact, collisions among smaller objects orbiting Pluto–Charon produce a ring of debris. On short time scales, viscosity within the ring broadens it into a disk with a radius  $a_d \approx 50\text{--}100 R_P$ . For typical debris disk masses  $M_d \approx 10^{19}\text{--}10^{21}$  g, collisions produce several satellites with masses comparable to those of P5–Hydra at semimajor axes reasonably close to the current orbits of the satellites. Once formed, satellites may migrate through the leftover debris. These results support the idea that satellites with masses comparable to those of P5, Nix, P4, and Hydra grow out of material in a circumbinary disk.

We develop the basic physical processes and calculate relevant time scales for this picture in §2. In §3, we describe time-dependent evolutionary calculations of a ring of debris surrounding Pluto or Pluto–Charon and its interaction with material orbiting the Sun (§3.1), summarize results of coagulation calculations for satellite growth (§3.2), and illustrate plausible migration scenarios (§3.3). We discuss the implications for the *New Horizons* mission (Stern 2008) and outline how additional calculations can improve and test our formation model in §4. We conclude with a brief summary in §5. To isolate basic conclusions from analytic estimates and numerical simulations, we use short summary paragraphs and subsections throughout the text. Table 1 lists the main symbols defined in the text. Table

2 summarizes the physical processes involved in the model and includes a reference to the appropriate section of the text.

## 2. PHYSICAL MODEL

To construct a predictive theory for the formation and evolution of the Pluto–Charon binary, we focus mainly on the giant impact scenario. In this picture, two massive protoplanets within the protoplanetary<sup>1</sup> debris disk collide and produce a binary planet embedded in a ring of debris. Aside from the basic idea of a giant impact, our discussion diverges from Earth–Moon models. Unlike the Earth–Moon event, (i) the impact of icy protoplanets does not form a disk of vapor and molten material, (ii) an object with roughly the mass of Charon survives the impact, and (iii) debris from the impact lies well outside the Roche limit of Pluto (Canup 2005, 2011, and references therein).

Our approach has some features in common with recent scenarios where coagulation in material just outside Saturn’s ring system leads to the formation of several of the innermost moons (e.g., Charnoz et al. 2010, 2011). Unlike Saturn, the evolution of the Pluto–Charon binary has a large impact on the formation and dynamical evolution of the satellites (e.g., Ward & Canup 2006; Lithwick & Wu 2008). The large velocity dispersion of debris from the Pluto–Charon impact also complicates coagulation calculations compared to Saturn’s rings, where the low velocity dispersion allows rapid growth once material escapes the Roche limit (Salmon et al. 2010; Charnoz et al. 2011).

Our calculations follow some aspects of the Ward & Canup (2010) method for deriving the formation and evolution of satellites within the circumplanetary disks of gas giant planets (see also Canup & Ward 2002; Sasaki et al. 2010; Ogihara & Ida 2012). Like Ward & Canup (2010), we consider the evolution of a viscous circumplanetary disk where small particles grow into satellites. For satellites around a gas giant, Ward & Canup (2010) derive the evolution of a circumplanetary disk of gas and dust fed from the surrounding protoplanetary disk. They include the growth and migration of satellites within the gaseous disk. For Pluto–Charon, the mass of the gaseous component of the disk is negligible. Thus, we consider the evolution of a pure particle disk. Instead of deriving the radial disk structure and the growth of satellites analytically, we employ a diffusion code to derive disk structure and we use a hybrid coagulation/ $n$ -body code to follow the growth and migration of satellites as a function of radial distance from the central binary (see also Ogihara & Ida 2012).

---

<sup>1</sup>Throughout this paper, we use ‘circumplanetary’ (‘circumbinary’) to refer to material orbiting a single (binary) planet and ‘protoplanetary’ to refer to material orbiting the Sun.

In this section, we develop the framework for analyzing the formation of the Pluto–Charon satellites within debris captured from the protoplanetary disk or retained after the giant impact. For the capture hypothesis, we derive estimates for the rate of capture and the equilibrium disk mass as a function of the properties of the protoplanetary disk and the capture efficiency. Our results suggest that capture is a viable mechanism to produce low mass satellites surrounding the Pluto–Charon binary.

For the giant impact hypothesis, we outline the evolution of debris following the impact. Using results for orbital stability in binary systems and simple estimates of evolutionary time scales for the Pluto–Charon binary and the debris, we conclude that Charon accretes 25% to 50% of the debris. The binary ejects the rest into a ring surrounding the binary. Because the number of 10–100 km objects in the debris is small, a few of them might avoid accretion by Charon and end up in the ring. Smaller objects probably suffer a few destructive collisions. Thus, the ring consists of, at most, a few large objects and many objects with  $R \lesssim 1$  km.

The evolution of material in the circumbinary ring depends on the relative importance of collisional damping, dynamical friction, and viscous spreading. As long as the central binary has a non-zero orbital eccentricity  $e_{PC}$ , material in the ring has a forced eccentricity  $e_f \approx e_{PC}$  (e.g., Heppenheimer 1974; Holman & Wiegert 1999; Wyatt et al. 1999; Lee & Peale 2006). In a narrow ring, collisions are destructive; the viscous time scale is shorter than the time scales for collisional damping and dynamical friction. Thus, the ring spreads into a disk. Once the disk has a radial width comparable to its semimajor axis, collisional damping becomes more effective. Collisions then produce larger objects. Although viscous spreading slows down, the disk continues to expand and may interact with material from the protoplanetary debris disk.

As the largest objects grow, they may migrate through the circumbinary disk. During this evolution, gravitational stirring dominates collisional damping. Stirring leads to a collisional cascade where the smallest objects are ground into small dust grains which are ejected from the system. Thus, growing satellites migrate through a disk with a slowly declining mass.

To derive the time scales and important physical issues for this scenario, we begin with estimates for the frequency of giant impacts in the protoplanetary disk. After concluding that these impacts are common, we demonstrate that a low-mass debris disk probably surrounded proto-Pluto prior to impact. We then consider (i) the evolution of debris immediately after the impact, (ii) the evolution of the expanding debris disk, (iii) interactions with the protoplanetary debris disk, and (iv) satellite migration through the circumbinary debris disk.

## 2.1. Impact Frequency

Throughout the history of the solar system, giant impacts are common. In the standard theoretical picture, icy and rocky protoplanets form by gradual accumulation of planetesimals, small solid objects with radii of 0.1–100 km (e.g., Greenberg et al. 1984; Wetherill & Stewart 1989; Kokubo & Ida 1996; Weidenschilling et al. 1997; Kenyon & Luu 1998; Kenyon 2002; Nagasawa et al. 2005; Kenyon et al. 2008). As long as the mass in planetesimals is larger than the mass in protoplanets, dynamical friction between the two sets of objects dominates viscous stirring among protoplanets (Goldreich et al. 2004). Thus, protoplanet orbital eccentricities remain small. Collisions among protoplanets are very rare. When protoplanets contain more than half of the total mass, viscous stirring dominates dynamical friction. Protoplanet eccentricities increase; chaotic growth begins. During chaotic growth, protoplanets grow through giant impacts with other protoplanets (e.g., Chambers 2001; Kominami & Ida 2002; Kenyon & Bromley 2006). Giant impacts remain common until protoplanets clear their orbits of other protoplanets and leftover planetesimals.

Outcomes of giant collisions among protoplanets depend on the impact parameter,  $b$ , and the impact velocity  $v_{imp}$  (Asphaug et al. 2006; Leinhardt et al. 2010; Canup 2011). Usually,  $v_{imp} \gtrsim v_{esc}$ , where  $v_{esc}$  is the mutual escape velocity of a merged pair of protoplanets. Head-on impacts with  $b \approx 0$  then produce mergers with little or no debris. Grazing impacts with  $b \approx 1$  yield two icy planets on separate orbits and some debris. When  $b \approx 0.7$ – $0.9$ , collisions often produce a binary planet – similar to the Earth–Moon or Pluto–Charon system – embedded in a disk or ring of debris.

The frequency of collisions that produce a binary planet depends on the distribution of possible impact parameters. During the late stages of evolution, the system of protoplanets is highly flattened (Wetherill & Stewart 1993; Weidenschilling et al. 1997; Chambers & Wetherill 1998; Kenyon & Bromley 2006, 2010). With most collisions in the plane of the disk, the frequency of various types of impacts is roughly the distribution of impact parameters. Assuming all impact parameters are equally likely, the probability that a collision will produce a binary planet is roughly the probability of an impact with  $b \approx 0.7$ – $0.9$ ,  $\sim 20\%$ .

### 2.1.1. Basic Model

To estimate the frequency of these impacts among icy objects during the early history of the solar system, we examine results from recent numerical calculations of planet formation at 15–150 AU around a solar-type star (Kenyon & Bromley 2008, 2010, 2012). In these calculations, we follow the evolution of protoplanets and planetesimals as a function of

semimajor axis  $a$  and time  $t$ . Calculations begin with an initial ensemble of planetesimals with maximum radius  $R_0$  and roughly circular orbits in a disk with a surface density of solids,

$$\Sigma(a) = \Sigma_0 x_m a^{-n}, \quad (1)$$

where  $\Sigma_0$  is a normalization factor designed to yield a surface density equivalent to the ‘minimum mass solar nebula’ at 1 AU (Weidenschilling 1977b; Hayashi 1981),  $x_m$  is a scaling factor to allow a range of initial disk masses, and  $n = 1-2$ .

To derive the outcomes of collisions among planetesimals and protoplanets, we use an energy-scaling approach where the outcome depends on the ratio  $Q_c/Q_D^*$ , where  $Q_c$  is the collision energy and  $Q_D^*$  is the energy required to disperse half the mass of a pair of colliding planetesimals to infinity. From detailed  $n$ -body and smooth particle hydrodynamics calculations (Benz & Asphaug 1999; Leinhardt et al. 2008; Leinhardt & Stewart 2009),

$$Q_D^* = Q_b R^{\beta_b} + Q_g \rho R^{\beta_g} \quad (2)$$

where  $Q_b R^{\beta_b}$  is the bulk component of the binding energy,  $Q_g \rho R^{\beta_g}$  is the gravity component of the binding energy, and  $R$  is the radius of a planetesimal. Table 3 lists the fragmentation parameters for the weak, strong, and very strong planetesimals with  $\rho = 1.5 \text{ g cm}^{-3}$  used in our calculations.

### 2.1.2. Results

Fig. 1 shows the frequency (number per Myr) of impacts with  $b = 0-1$  as a function of time for calculations with strong planetesimals ( $R_0 = 1 \text{ km}$ ) and with several initial surface density distributions. In each panel, the curves plot the frequency of impacts between a target with mass  $M_t \gtrsim 10^{25} \text{ g}$  and a projectile with a mass  $M_p \gtrsim q_p(M_t + M_p)$  where  $q_p = 0.25$ . As summarized in the caption, color indicates the semimajor axis of a disk annulus, ranging from 30–36 AU (violet) to 120–150 AU (black). Left-hand panels show results for disks with  $x_m = 0.10-0.33$  and  $n = -1.0$ ; right-hand panels plot results for disks with  $x_m = 1.00-3.00$  and  $n = -1.5$ . Disks with  $(n, x_m) = (-1.0, 0.33)$  and  $(-1.5, 3.00)$  have the roughly the same total disk mass (see Kenyon & Bromley 2010).

These results demonstrate that giant impacts are common throughout the evolution of the solar system (see also McKinnon 1989; Canup 2005, 2011). Initially, all planetesimals are smaller than the target mass; the frequency of giant impacts is zero. As planetesimals grow into large protoplanets, the frequency of giant impacts increases. Because protoplanets grow faster in the inner disk than in the outer disk (Kenyon & Bromley 2004a,b), giant impacts occur earlier in the inner disk (violet and blue curves) than in the outer disk (magenta and

black curves; see also Kenyon & Bromley 2005). In each disk annulus, the giant impact frequency rapidly rises to a clear peak when the surface density of targets and projectiles is largest. As large objects collide and merge into larger protoplanets, the giant impact frequency declines. The rate of decline,  $p_i \propto t^{-1}$ , is the rate expected for collisional evolution in a protoplanetary disk (Kenyon & Bromley 2002; Dominik & Decin 2003; Wyatt 2008).

Several factors contribute to the strong variation of  $p_i$  with initial disk mass. In these calculations, the number of Pluto-mass objects  $N_P$  grows with increasing disk mass, with  $N_P \propto x_m$  (Kenyon & Bromley 2008, 2012). For giant impacts requiring two Pluto-mass objects, the number of possible pairs of impactors scales with the square of the disk mass. In more massive disks, the larger mass of leftover planetesimals circularizes the orbits of the largest planets more effectively. Thus, gravitational focusing factors also scale with disk mass. Combining these two factors, the impact probability grows rapidly with disk mass,  $p_i \propto x_m^n$ , with  $n \approx 3-4$ .

Finally, the frequency of giant impacts depends on the initial size and strength of planetesimals (Fig. 2). In the left panels of Fig. 2, calculations with weak planetesimals yield a much lower frequency of giant impacts than calculations with strong planetesimals. When planetesimals are strong or very strong, high velocity collisions produce very little debris (Kenyon & Bromley 2004c, 2010, 2012). Thus, the mass reservoir to produce Pluto-mass protoplanets declines slowly with time. When planetesimals are weak, collisions produce copious amounts of debris (Kenyon & Bromley 2010); the mass reservoir declines rapidly with time. With less mass to produce massive protoplanets, calculations with weak planetesimals produce fewer massive protoplanets. Fewer massive protoplanets yield a smaller giant impact frequency.

Although increasing  $R_0$ , the initial maximum size of planetesimals, has little impact on the maximum frequency of giant impacts, calculations with larger  $R_0$  produce giant impacts later in the evolution than calculations with smaller  $R_0$  (Fig. 2, right panels). Large planetesimals stir their surroundings more effectively and require longer time scales to grow to 1000 km than small planetesimals (Kenyon & Bromley 2010, 2012).

Despite the large range in the giant impact frequency for different initial collisions, all calculations yield  $p_i \gtrsim 0.01 \text{ Myr}^{-1}$  at 15–30 AU and  $p_i \gtrsim 0.001 \text{ Myr}^{-1}$  at 40–60 AU. If the distribution of impact parameters is random, the frequency of binary planets is  $p_{bp} \approx 0.2p_i$ . Thus, the frequency of giant impacts capable of producing a binary planet exceeds 1 per 100–300 Myr at 30 AU. At 20 AU (40 AU), the typical frequency is roughly a factor of two larger (smaller).



### 2.1.3. Summary: Giant Impacts are Common

We conclude that giant impacts capable of producing the Pluto–Charon binary can occur at any semimajor axis  $a \approx 20\text{--}40$  AU prior to 0.5–1 Gyr. Although calculations starting with 1–10 km planetesimals produce binary planets earlier in time than calculations with 100 km planetesimals, Pluto–Charon binaries are a likely outcome of planet formation in massive disks.

For the rest of this section, we assume a protoplanetary disk similar to the MMSN, with  $n = 3/2$  and  $\Sigma_0 = 30 \text{ g cm}^{-2}$ . As long as the disk is massive enough to produce a reasonably high frequency of giant impacts, other choices lead to similar conclusions.

## 2.2. Circumplanetary Debris Disk Evolution: Before and After Impact

In addition to the two protoplanets involved in the Pluto–Charon-forming giant impact, the protoplanetary disk contains a large ensemble of other protoplanets, leftover planetesimals, and small dust grains. Although protoplanets sweep up this debris inefficiently, material can interact within the Hill sphere of the protoplanet and form a circumplanetary debris disk (e.g., Weidenschilling 2002; Goldreich et al. 2002). Once a circumplanetary disk forms, material orbiting the planet may interact with other material passing through the Hill sphere (e.g., Durda & Stern 2000; Stern 2009; Pires dos Santos et al. 2012).

The Hill radius,  $R_H$ , defines a spherical surface where the gravity of a planet roughly balances the gravity of the Sun. For a planet with mass density  $\rho$  orbiting the Sun at semimajor axis  $a_\odot$ :

$$R_H \approx 4 \times 10^6 \left( \frac{R}{R_P} \right) \left( \frac{\rho}{2 \text{ g cm}^{-3}} \right)^{1/3} \left( \frac{a_\odot}{20 \text{ AU}} \right) \text{ km} . \quad (3)$$

When an object from the protoplanetary disk enters the Hill sphere, there are four possible outcomes:

- It can interact with Pluto–Charon, find a temporary orbit, and collide with other objects on similar orbits (Pires dos Santos et al. 2012). Because the collision time is much longer than the lifetime in a captured orbit, captured material probably cannot form a circumplanetary disk. Thus, we do not consider this option.
- It can collide with another object from the protoplanetary disk (e.g., Weidenschilling 2002; Kominami et al. 2011). This collision yields a single large object and some debris.

If this material can lose enough kinetic energy to achieve an orbit with semimajor axis  $a \lesssim \gamma R_H$  and  $\gamma \approx 0.4$ , it may become bound to the protoplanet. Solids with  $\gamma > 0.4$  cannot execute closed orbits around the planet and are eventually ejected (e.g. Martin & Lubow 2011).

- It can collide with an object in the circumplanetary disk. During the late stages of planet formation, incoming projectiles have much larger velocities than target objects orbiting within the disk. If the projectile has a mass much smaller than the target, the target – and other nearby objects within the disk – accrete most of the incoming material (e.g., Durisen et al. 1989; Stern 2009; Housen & Holsapple 2011). Projectiles with masses much larger than the target remove material from the disk.
- It can pass through the Hill sphere without any collision. When the optical depths of the circumplanetary and protoplanetary disks are smaller than unity, this outcome is the most likely one.

For simplicity, we first assume that material entering the Hill sphere at a distance  $a \lesssim \gamma R_H$  from the planet can interact with other objects and remain bound. This material encounters the Hill sphere at a rate  $\dot{M}_d \approx 3\pi\Sigma_\odot\Omega_\odot(\gamma R_H)^2$ , where  $\Sigma_\odot$  is the surface density of the protoplanetary disk,  $\Omega_\odot$  is the angular velocity of the planet around the Sun, and the factor of three accounts for a small degree of gravitational focusing<sup>2</sup> (see also Weidenschilling 2002; Kennedy & Wyatt 2011). Adopting conditions appropriate for a proto-Pluto, this rate is

$$\dot{M}_d \approx 5 \times 10^{21} f_\odot x_m \left( \frac{a_\odot}{20 \text{ AU}} \right)^{-1} \text{ g yr}^{-1}, \quad (4)$$

where we include a factor  $f_\odot$  to account for time-dependent depletion of the initial surface density distribution.

The probability that an object in the Hill sphere interacts with other objects is roughly  $\tau_d + \tau_p$ , the sum of the optical depths of the circumplanetary and the protoplanetary disk. With  $\tau \approx \Sigma/R$ , we estimate

$$\tau_p \approx 3 \times 10^{-8} f_\odot x_m \left( \frac{R_{max}}{100 \text{ km}} \right)^{-1} \left( \frac{a_\odot}{20 \text{ AU}} \right)^{-3/2}, \quad (5)$$

where  $R_{max}$  is the radius of a typical large object in the protoplanetary disk.

For the circumplanetary disk, the optical depth for particles moving through the Hill sphere is  $\tau_d \approx (\Sigma/R)(H_z/a)$ , where  $H_z = v_z\Omega^{-1}$  is the vertical scale height and  $v_z$  is

---

<sup>2</sup>During this epoch, the vertical scale height of the disk,  $H_\odot$ , is much larger than  $R_H$ .

the vertical velocity dispersion. Usually,  $v_z$  is half the radial velocity dispersion  $v_r$  (e.g., Hornung et al. 1985; Ohtsuki 1992; Ida et al. 1993). The radial velocity dispersion is roughly the escape velocity of the largest solid objects in the disk (e.g., Barge & Pellat 1990; Kokubo & Ida 1995; Kenyon & Bromley 2001; Goldreich et al. 2004). If the largest objects have radius  $R_d$  and mass density  $\rho \approx 1 \text{ g cm}^{-3}$ ,

$$v_r \approx 53 \left( \frac{R_d}{1 \text{ km}} \right) \text{ cm s}^{-1} . \quad (6)$$

The optical depth in the circumplanetary disk for collisions with material in the protoplanetary debris disk is then independent of particle size:

$$\tau_d \approx 10^{-10} \left( \frac{M_d}{10^{20} \text{ g}} \right) \left( \frac{a_\odot}{20 \text{ AU}} \right)^{-3} , \quad (7)$$

where  $M_d$  is the total mass of the disk.

To estimate the probability that collisions within the Hill sphere yield some material bound to the planet, we first consider the fate of two objects from the protoplanetary disk (see also Weidenschilling 2002; Goldreich et al. 2002). Most material interacts near the outer edge of the disk at  $\gamma R_H$  where the orbital velocity around the planet is  $v_{orb} \approx 2000 \text{ cm s}^{-1}$ . With typical impact velocities exceeding  $\sim 2 \times 10^4 \text{ cm s}^{-1}$ , a single object must lose roughly 99% of its kinetic energy to remain bound. In his analysis of the formation of binaries in the Kuiper belt, Weidenschilling (2002) derives capture probabilities of 0.1% to 1%. For conditions in a young protoplanetary disk, Goldreich et al. (2002) explore whether dynamical friction or three-body interactions allow capture. They conclude that  $\sim 3\%$  of incoming material can remain bound to the protoplanet. At times when giant impacts are common, dynamical friction is more than a factor of ten less effective. Reducing the impact of dynamical friction implies a capture probability of  $\lesssim 0.3\%$ , comparable to the Weidenschilling (2002) estimate.

For incoming planetesimals colliding with material already in the circumplanetary disk, depletion is much more likely than capture. Because the disk is mainly collision debris, incoming planetesimals are much larger than objects within the disk. Typical collisions between an incoming planetesimal and an orbiting target then produce an impact crater on the planetesimal and some ejecta from the target. For an incoming planetesimal with  $R \approx 10\text{--}100 \text{ km}$  and a target with  $0.1\text{--}1 \text{ km}$ , the mass in the ejecta is less than a few per cent the mass of the target (e.g., Housen & Holsapple 2011, and references therein). Although circumplanetary objects may accrete the ejecta (e.g., Stern 2009; Poppe & Horányi 2011), the incoming planetesimal escapes with most of the mass of the target and depletes the circumplanetary disk.

When incoming objects have small masses, collisions add material to the circumplanetary disk (e.g., Durisen et al. 1989; Stern 2009; Poppe & Horányi 2011). However, objects

with  $R \lesssim 0.1$  km contain much less than 1% of the mass of the protoplanetary disk. Thus, incoming low mass objects add relatively little mass to the circumplanetary disk.

In steady-state, depletion from high velocity collisions with the disk balances the addition of debris from collisions within the Hill sphere. Defining  $f_d$  as the fraction of debris captured by the planet, steady-state implies  $f_d \tau_p \approx \tau_d$ . Solving for the state-state disk mass:

$$M_d \approx 3 \times 10^{19} f_\odot x_m \left( \frac{f_d}{10^{-3}} \right) \left( \frac{R_{max}}{100 \text{ km}} \right)^{-1} \left( \frac{a_\odot}{20 \text{ AU}} \right)^{3/2} \text{ g}. \quad (8)$$

Viscosity within the disk probably transports mass inward onto the central planet and outward through the Hill sphere. Thus, this disk mass is a rough upper limit. With a typical input rate of roughly  $10^{11} \text{ g yr}^{-1}$ , it takes at least 30–100 Myr to reach this steady-state disk mass.

As long as the protoplanetary disk has a surface density reasonably close to its initial value, Pluto-mass planets can sustain modest circumplanetary disks of solid material. This mass is roughly at the lower limit for the sum of the masses of the known satellites surrounding Pluto–Charon. Growth of planets or satellites is rarely 100% efficient (e.g., Kenyon & Bromley 2004a, 2008, 2010, 2012). Unless capture is more efficient than our simple estimates, forming massive satellites around Pluto–Charon requires an additional source of material. The giant impact which produces Charon is the most likely source of this material.

### 2.3. Immediate Aftermath

After the impact, the Pluto–Charon binary and the surrounding debris evolve on various time scales. Initially, the binary has semimajor axis  $a_{PC} \approx 5\text{--}10 R_P$  and eccentricity  $e_{PC} \approx 0.1\text{--}0.8$  (Canup 2011). The initial orbital period sets the shortest time scale in the system:

$$T_{PC} \approx \left( \frac{a_{PC}}{5 R_P} \right)^{3/2} \text{ d}. \quad (9)$$

Debris from the impact mostly lies in an elliptical ring along Charon’s orbit. For a binary with mass ratio  $q = 0.1$ , the minimum semimajor axis for stable orbits outside the binary is (Holman & Wiegert 1999)

$$a_{min} = (1.96 + 4.68e - 2.17e_{PC}^2) a_{PC} . \quad (10)$$

For  $e_{PC} = 0.1\text{--}0.8$ , test particle orbits with  $a_{min} \lesssim 2.4\text{--}4.3 a_{PC}$  are unstable. Any debris inside  $a_{min}$  is accreted by the binary pair or ejected into orbits outside the binary. Material

outside the binary likely collects in a ring with orbital semimajor axis  $a_d \gtrsim a_{min}$ . This material has a minimum orbital period

$$T_{d,min} \approx 4 - 9 \left( \frac{a_{PC}}{5 R_P} \right)^{3/2} \text{ d} . \quad (11)$$

If the debris from the impact is distributed fairly smoothly along the orbit, Charon accretes this material at a rate  $\dot{M}_C \approx \Sigma \Omega_{PC} R_C^2 \approx 0.1 M_d T_{PC}^{-1}$ , where  $R_C$  is the radius of Charon and  $\Omega_{PC}$  is the angular velocity of the Pluto–Charon binary. The time scale to sweep up all of the debris is

$$t_{acc} = M_d / \dot{M}_C \approx 10 \left( \frac{a_{PC}}{5 R_P} \right)^{3/2} \text{ d} . \quad (12)$$

The fraction of debris particles accreted by Charon depends on the time scale to eject material from the vicinity of the binary. Dynamical simulations of particles along Charon’s orbit suggest it takes a few orbital periods to accrete or to eject particles from the vicinity of the binary system. Thus, Charon probably accretes 25% to 50% of the debris along its orbit. The Pluto–Charon binary ejects the rest. To conserve energy and angular momentum, the Pluto–Charon binary contracts. For a mass in debris,  $M_d \approx 10^{20}$  g at  $a_{min}$ , the decrease in the Pluto–Charon orbital period is much smaller than 1%.

As Pluto–Charon eject particles beyond  $a_{min}$ , collisions among debris particles help to circularize their orbits. If the debris maintains a fairly smooth surface density along the orbit, the collision rate is  $dn/dt \approx (M_d / \pi \delta a_{PC}^2) \Omega_{PC} / \rho R$ , where  $\delta$  is the width of the ring and  $R$  is the radius of an object in the debris. With  $\rho = 1 \text{ g cm}^{-3}$ , the collision time is

$$t_c = (dn/dt)^{-1} \approx 3 \left( \frac{\delta}{0.1} \right) \left( \frac{R}{0.1 \text{ km}} \right) \left( \frac{10^{20} \text{ g}}{M_d} \right) \left( \frac{a_{PC}}{5 R_P} \right)^{7/2} \text{ d} . \quad (13)$$

For a mass,  $M_d \approx 10^{20}$  g, the collision time for 10 km and larger particles exceeds the time scale for Charon to eject or to sweep up the debris. Thus, large proto-satellites can escape the Pluto–Charon binary more or less intact.

While Charon ejects or sweeps up the debris, smaller particles suffer destructive collisions. Around the Pluto–Charon binary, typical orbital velocities are  $0.5 \text{ km s}^{-1}$ . With initial  $e = 0.1$ – $0.8$ , impact velocities are roughly  $100 \text{ m s}^{-1}$ . Impact energies exceed  $10^7 \text{ erg g}^{-1}$ . Collisions involving particles with  $R \sim 0.3$ – $5 \text{ km}$  are completely disrupted; among  $10$ – $30 \text{ km}$  objects, cratering collisions reduce the mass by roughly 5% ( $30 \text{ km}$ ) to 25% ( $10 \text{ km}$ ) per collision (see, for example, Leinhardt et al. 2010; Kenyon & Bromley 2012). For  $M_d \approx 10^{20}$  g and the

collision time in eq. (13), mutual collisions among particles with  $R \lesssim 5$  km ( $M \lesssim 5 \times 10^{17}$  g for  $\rho \approx 1$  g cm $^{-3}$ ) produce an ensemble of smaller particles orbiting the Pluto–Charon binary.

As Charon ejects debris, collisional damping effectively circularizes the orbits of the smallest objects. For objects with  $R \lesssim 0.1$  km, the damping time is comparable to or smaller than the orbital period of the Pluto–Charon binary (e.g., eq. 13; see also Goldreich et al. 2004). Efficient damping leaves the debris on roughly circular orbits with semimajor axes,  $a_d \approx a_{min}$ .

Because collisions among large objects are infrequent (eq. [13]), their orbits are circularized by dynamical friction or by direct erosive collisions with the smaller objects (e.g., Goldreich et al. 2004). Following the impact, particle velocities exceed the escape velocity of 10–30 km objects. Thus, dynamical friction is in the dispersion regime where gravitational focusing factors are roughly 1. The damping time scale for dynamical friction is then  $t_{df} \approx (R/\Sigma_s)T_{PC}$ , where  $\Sigma_s$  is the surface density of the small particles. If small particles contain a fraction  $f_s$  of the initial mass, the damping time scale is

$$t_{df} \approx 3f_s \left( \frac{\delta}{0.1} \right) \left( \frac{R}{0.1 \text{ km}} \right) \left( \frac{10^{20} \text{ g}}{M_d} \right) \left( \frac{a_{PC}}{5 R_P} \right)^{7/2} \text{ d} . \quad (14)$$

Dynamical friction circularizes the orbits of large particles on long time scales compared to the orbital time of the binary. Because collisions with small particles erode the large particles on similar time scales, large particles may not survive the circularization process.

Interactions with any pre-existing circumplanetary debris disk also circularize the orbits of impact debris. Dynamical friction and collisional damping reduce the radial velocity dispersion of the impact debris. With a typical mass of  $\sim 10^{19}$  g spread over  $1000 R_P$ , the pre-existing disk has an angular momentum roughly 10 times larger than the initial angular momentum of the impact debris. Circularizing the orbits of impact debris beyond  $a_{min}$  requires a modest reduction in the angular momentum of pre-existing disk material. The time scale to circularize the orbits of the 0.1–1 km particles in debris is roughly the collision time,  $\sim 0.1$ –1 yr.

We conclude that the Pluto–Charon binary ejects debris into a ring with a typical semimajor axis  $a_d \gtrsim a_{min}$ . For simplicity, we set  $a_d \approx 4a_{PC} \approx 20R_P$ . The solid material in the ring consists primarily of small particles with  $R \lesssim 1$  km and perhaps a few larger objects with  $R \gtrsim 10$  km. The evolution of the central binary then depends on tidal processes between Pluto–Charon (e.g., Dobrovolskis et al. 1997) and gravitational interactions between Pluto–Charon and the surrounding ring of debris.

## 2.4. Orbital Evolution of the Central Binary

Over long time scales, tidal interactions between Pluto and Charon modify the orbit and rotation of the binary (Dobrovolskis et al. 1997). Following Peale (1999), the rate of change of the angular rotational velocity,  $\omega$ , of Charon is  $\dot{\omega} \approx (-45/76)(\rho\Omega^4 R_C^2/\mu Q)\text{sign}(\omega - \Omega)$ , where  $1/Q$  is the angular phase lag in the tidal oscillation and  $\mu$  is the rigidity. Holding the structure of Pluto–Charon fixed at  $Q \approx 100$  and  $\mu \approx 4 \times 10^{10}$  dyne cm<sup>-2</sup>, the time scale to synchronize  $\omega$  is

$$t_{sync} \approx 170 \left( \frac{a_{PC}}{a_{PC,0}} \right)^6 \left( \frac{1 \text{ d}}{t_{r,0}} - \frac{1 \text{ d}}{t_r} \right) \text{ yr} , \quad (15)$$

where  $t_r$  is the rotational period, and  $t_{r,0}$  is the initial rotational period. Thus, Charon’s rotation synchronizes rapidly with the orbit on a time scale,  $t_{sync} \approx 10^2\text{--}10^4$  yr for  $a_{PC} \approx 5\text{--}10 R_P$ .

Tidal interactions also expand the orbit. Tides change the angular orbital frequency at a rate  $\dot{\Omega} \approx (-9/2)(kM_C R_P^5 \Omega^{16/3}) / (QM_P [G(M_P + M_C)]^{5/3}) \text{sign}(\omega - \Omega)$  (Peale 1999), where  $k \approx 9.4 \times 10^{-3}$  is the Love number for the potential (Love 1944; Peale 1999). If the structural parameters are held fixed, tides slowly expand the Pluto–Charon semimajor axis:

$$a_{PC} = a_{PC,0} \left( 1 + \frac{t}{t_{exp}} \right)^{6/39} , \quad (16)$$

where the expansion time is  $t_{exp} \approx 6500(a_{PC,0}/5R_P)^{39/6}$  yr. From an initial semimajor axis  $a_{PC,0} \approx 5\text{--}10 R_P$ , the orbit evolves to the current  $a_{PC} = 17 R_P$  in 0.2–20 Myr (see also Farinella et al. 1979; Dobrovolskis et al. 1997).

Dynamical interactions with the circumbinary debris disk help to circularize the Pluto–Charon orbit, but they slow orbital expansion. For a ring of material with  $a_d \approx 20R_P$  surrounding a Pluto–Charon binary with  $a_{PC} \approx 5R_P$  and  $e_{PC} \approx 0.1$ , numerical simulations with the *Orchestra* code (see §3.3) suggest

$$\dot{e}_d \approx -2.5 \times 10^{-7} \left( \frac{M_d}{10^{20} \text{ g}} \right) \text{ yr}^{-1} \quad (17)$$

and

$$\dot{a}_d \approx -2 \times 10^{-5} \left( \frac{M_d}{10^{20} \text{ g}} \right) R_P \text{ yr}^{-1} . \quad (18)$$

When the debris disk has a mass comparable to the masses of the satellites, the time scale for dynamical interactions to change  $a$  and  $e$  is similar to the tidal time scale.

## 2.5. Initial evolution of debris ring

### 2.5.1. The ring spreads

Once material lies in a ring outside the Pluto–Charon binary, collisional processes within the ring are more important than the dynamical evolution of the binary. Tidal forces from the binary truncate the disk (e.g., Lin & Papaloizou 1979; Pringle 1991) and impose a forced eccentricity,  $e_f \approx e_{PC}$ , on ring particles (e.g., Murray & Dermott 1999; Wyatt et al. 1999; Lee & Peale 2006; Tsukamoto & Makino 2007). The time scales for these interactions (eqs. [13] and [14]) are much smaller than the  $10^5$ – $10^7$  yr time scale for tidal interactions to circularize and to expand the orbit (Dobrovolskis et al. 1997).

Viscous spreading occurs on a time scale  $t_\nu \approx (\delta a)^2/\nu$  where  $\nu$  is the viscosity (Lynden-Bell & Pringle 1974; Pringle 1981). For a disk of identical indestructible particles undergoing inelastic collisions, the viscosity is roughly (Goldreich & Tremaine 1982)

$$\nu \approx \frac{v_r^2}{\Omega} \frac{0.46\tau}{1 + \tau^2}, \quad (19)$$

where  $\tau \approx 3\Sigma/4R\rho$  is the optical depth of the ring.

When  $\tau$  is small, gravitational scattering augments the collisional viscosity (Shu & Stewart 1985; Hornung et al. 1985). The viscosity from gravitational encounters is roughly (Hornung et al. 1985)

$$\nu_s \approx 0.5 \frac{v_{esc}^2}{\Omega} \frac{v_{esc}^2}{v_r^2} L\tau, \quad (20)$$

where  $v_{esc}$  is the escape velocity of the particles and  $L = \ln(H_z/2R) \approx 3$ – $5$ . In an equilibrium disk,  $v_r \lesssim v_{esc}$  (Hornung et al. 1985; Barge & Pellat 1990). The gravitational scattering component of the viscosity then exceeds the collisional component by a factor of 3–10 (see also Hornung et al. 1985).

Initially, particles in the ring have large velocity dispersions set by the dynamics of the central binary. The gravitational component of the viscosity is then much smaller than the collisional component. With  $v_r \approx e_{PC} \Omega a_d$ , the viscous time during the early parts of the evolution is

$$t_\nu \approx 650 \left( \frac{R}{0.1 \text{ km}} \right) \left( \frac{M_d}{10^{20} \text{ g}} \right)^{-1} \left( \frac{e}{0.1} \right) \left( \frac{a_d}{20 R_P} \right)^{7/2} \text{ d}. \quad (21)$$

With an initial viscous time of 1–2 yr, the ring spreads rapidly.

The ratio of the collision time to the viscous time is

$$\left( \frac{t_c}{t_\nu} \right)_{init} \approx \frac{1}{2} \left( \frac{v_r}{\Omega \delta a_d} \right)^2. \quad (22)$$



For a narrow ring with  $v_r \approx e_{PC} \Omega a_d$  and  $\delta a_d/a_d \approx e_{PC}$ , the collision and viscous times are roughly equal. Each particle suffer several destructive collisions as the ring spreads.

### 2.5.2. Particle sizes in the ring

When destructive collisions dominate, small particles are ground down into smaller and smaller objects. Radiation pressure can eject very small particles with  $R \approx 1\text{--}100 \mu\text{m}$  on the local orbital time scale; Poynting-Robertson drag pulls particles into the central star or planet on much longer time scales. For particle orbits around the Sun, a balance between radiation pressure and gravity establishes an absolute minimum size (Burns et al. 1979):

$$R_{min,\odot} \approx \frac{0.6 \mu\text{m}}{\beta \rho}, \quad (23)$$

where  $\rho$  is the mass density of a particle and  $\beta$  is the ratio of radiation pressure to gravity. Solar radiation pressure ejects particles with  $\beta \gtrsim 0.5\text{--}1$ ; thus  $R_{min} \approx 0.5\text{--}1 \mu\text{m}$  for icy particles with  $\rho \approx 1 \text{ g cm}^{-3}$ .

For orbits around a planet, the Sun ejects particles when radiation pressure exceeds the gravity of the planet (Burns et al. 1979). For Pluto–Charon, the minimum particle size increases by more than an order of magnitude<sup>3</sup>,

$$R_{min,PC} \approx 20 \left( \frac{a}{4a_{PC}} \right)^{1/2} \left( \frac{20 \text{ AU}}{a_{\odot}} \right)^{1/2} \mu\text{m}, \quad (24)$$

where  $a_{\odot}$  is the orbital semimajor axis of Pluto–Charon around the Sun. For the Pluto–Charon binary, particles with  $R \lesssim 0.5\text{--}1 \mu\text{m}$  are ejected from the binary and the solar system. Particles with  $R \approx 1\text{--}20 \mu\text{m}$  are ejected from the binary but remain bound to the Sun (see also Poppe & Horányi 2011).

Despite the increased efficiency of radiation pressure in removing small particles from a circumplanetary disk, Poynting-Robertson drag is ineffective. For particles with  $\rho \approx 1 \text{ g cm}^{-3}$  on Sun-centered orbits, the time scale for Poynting-Robertson drag to pull particles radially inward is

$$t_{PR} \approx 3 \times 10^5 \left( \frac{R}{1 \mu\text{m}} \right) \left( \frac{a_{\odot}}{20 \text{ AU}} \right) \text{ yr}. \quad (25)$$

---

<sup>3</sup>We assume radiation pressure ejects particles when  $\beta \approx v/v_{\odot}$ , where  $v$  is the orbital velocity around the planet and  $v_{\odot}$  is the orbital velocity of the planet around the Sun. Numerical simulations suggest this limit is appropriate for a disk of small particles where collisional damping counteracts radiation pressure.

For orbits around Pluto–Charon, the drag time is roughly 30% longer (Burns et al. 1979). Small particles with stable orbits around Pluto–Charon,  $R \gtrsim 20 \mu\text{m}$ , spiral toward the central binary on time scales comparable to the time scale for tidal evolution of the central binary. These particles probably cannot pass inside the tidal boundary of the binary at roughly  $a \gtrsim 2a_{PC}$ . Thus, small particles are likely swept up by large planetesimals close to the central binary.

Initially, the largest object in the ring has a radius  $R \lesssim 10\text{--}30 \text{ km}$  ( $m \lesssim 3\text{--}100 \times 10^{18} \text{ g}$ ). Disruptive collisions can reduce these objects in mass by a factor of ten. Thus, the maximum size is roughly 1–10 km. If all large objects suffer destructive collisions, the maximum size is close to 0.1 km. Near the binary, the smallest particles have radii of roughly  $20 \mu\text{m}$ . In this size range,  $20 \mu\text{m} < R < 0.1 - 10 \text{ km}$ , collisional evolution probably produces a differential size distribution  $n(r) \propto r^{-3.5}$  (e.g., Dohnanyi 1969; Williams & Wetherill 1994, but see also Belyaev & Rafikov 2011). Thus, most of the mass is in the largest objects.

### 2.5.3. After the ring spreads

As the ring spreads, collisional damping becomes more effective. The radial velocity dispersion declines. In this regime, the Hill radius,  $R_H$ , sets the length scale. Scaling eq. (3) to the size of the Pluto–Charon binary,

$$R_H \approx 10 \left( \frac{R}{1 \text{ km}} \right) \left( \frac{a}{20 R_P} \right) \text{ km} . \quad (26)$$

If a few large particles with  $R \gtrsim 10 \text{ km}$  survive dynamical ejection into the ring, they have Hill radii of 0.1–0.3  $R_P$ . These objects stir up material within a few Hill radii,  $\approx 0.3 - 1 R_P$ , of their orbits (e.g., Ida & Makino 1993; Ohtsuki et al. 2002). Because the initial width of the ring is a few Pluto radii, a few large particles can stir the entire ring. Although small particles with  $R \lesssim 0.1 - 1 \text{ km}$  have much smaller Hill radii, they are very numerous. In a ring with mass  $M_d \approx 10^{20} \text{ g}$ , small particles can also stir up the entire ring (e.g., Kokubo & Ida 1995; Kenyon & Bromley 2001).

When particle stirring dominates collisional damping, the minimum radial velocity dispersion is roughly the escape velocity of the largest objects, eq. (6) (Barge & Pellat 1990; Kokubo & Ida 1995; Kenyon & Bromley 2001; Goldreich et al. 2004). Small ring particles have vertical velocity dispersions of roughly half the radial velocity dispersion,  $v_z \approx v_r/2$ . The vertical scale height of the ring,  $H_z = v_z \Omega^{-1}$ , is:

$$H_z \approx 30 \left( \frac{R_{max}}{1 \text{ km}} \right) \left( \frac{a}{20 R_P} \right)^{3/2} \text{ km} . \quad (27)$$

The typical vertical height of the particle disk is smaller than a Pluto radius.

When  $\delta a_d/a_d \approx 1$  and  $v_r \approx v_{r,min}$ , the ratio of the collision time to the viscous time is:

$$\frac{t_c}{t_\nu} \approx 2.5 \times 10^{-3} \left( \frac{R}{1 \text{ km}} \right)^2 \left( \frac{20 R_P}{a_d} \right)^{1/2}. \quad (28)$$

If no large fragments with  $R \gtrsim 10$  km survive the giant impact, growth is faster than viscous spreading. The typical growth time is

$$t_c \approx 50 \left( \frac{R}{1 \text{ km}} \right) \left( \frac{10^{20} \text{ g}}{M_d} \right) \left( \frac{a_d}{15 R_P} \right)^{7/2} \text{ yr}. \quad (29)$$

Thus, the largest particles grow rapidly to 10–30 km.

After the largest objects reach radii of 10–30 km, the time scales for growth and viscous spreading are roughly equal. As viscosity continues to expand the ring into a disk, the largest objects continue to accrete smaller debris particles. Eventually, the disk consists of a few large objects orbiting the Pluto–Charon binary.

## 2.6. Migration Through the Circumbinary Disk

Although viscous spreading and collisional processes probably dominate the early evolution, gravitational scattering plays an important role in the local structure of the disk. Large objects try to clear their orbits by scattering smaller objects. Viscous spreading among smaller objects tries to fill the orbits of the larger objects. When the large objects dominate, they reduce the surface density along their orbits and increase the surface density outside their orbits. Because the surface density enhancements are not smooth, the large objects feel a torque from the small objects. If the sum of all of the torques does not vanish, the large objects migrate radially inward or outward (e.g., Goldreich & Tremaine 1982; Ward 1997; Kirsh et al. 2009).

When scattering overcomes viscous spreading, large objects can open gaps in the radial distribution of planetesimals. For convenience, we define the Hill radius necessary for a particle to open up a gap in a dynamically cold disk. For the Pluto–Charon binary, this radius is (e.g., Rafikov 2001; Bromley & Kenyon 2013)

$$R_{gap} \approx 15 \left( \frac{v_r}{53 \text{ cm s}^{-1}} \right)^{2/3} \left( \frac{M_d}{10^{20} \text{ g}} \right)^{1/3} \left( \frac{R}{1 \text{ km}} \right)^{-1/3} \left( \frac{a_c}{20 R_P} \right)^{1/3} \text{ km} \quad (30)$$

Objects with  $R_H \approx 15$  km have physical radii  $R \approx 1$  km (eq. [26]). For circumbinary disks with  $M_d \approx 10^{20}$  g, satellites with  $R \gtrsim 1$  km open gaps in the disk. All four Pluto–Charon satellites have  $R \gtrsim 3$  km. Thus, each can open a gap in a cold circumbinary disk.

For satellites with  $R \gtrsim R_{gap}$ , there are two possible modes of migration (e.g., Bromley & Kenyon 2011b, 2013). If the satellite can clear a gap in its corotation zone and migrate across this gap in one synodic period, the satellite undergoes fast migration. Satellites with Hill radii in the range  $R_{gap} < R_H < R_{fast}$  satisfy this condition. For the Pluto–Charon binary,

$$R_{fast} \approx 20 \left( \frac{M_d}{10^{20} \text{ g}} \right)^{1/2} \left( \frac{a}{20 R_P} \right)^{3/2} \text{ km.} \quad (31)$$

Depending on the disk properties and satellite location, this Hill radius corresponds to objects with physical radii of a few kilometers. Coupled with the limits on  $R_{gap}$ , satellites with physical radii of 1–5 km undergo fast migration. These objects drift radially inward or outward at a rate

$$\dot{a}_{fast} \approx \pm 5 \left( \frac{M_d}{10^{20} \text{ g}} \right) \left( \frac{a}{20 R_P} \right)^{3/2} \text{ km yr}^{-1}. \quad (32)$$

With minimum radii of 12 km (Nix) and 15 km (Hydra), the two massive satellites of Pluto–Charon are too massive to undergo fast migration. If the smaller P4 and P5 have albedo  $A \gtrsim 0.5$ , they are small enough to migrate in the fast mode.

Massive satellites that open up a gap in the disk migrate through the disk at a rate that depends on the disk viscosity. In gaseous disks with a large viscosity, this type II migration can transport gas giants from 5–10 AU to within a few stellar radii of a solar-type star in  $\sim 1$  Myr (Lin & Papaloizou 1986b; Ward 1997; Nelson & Papaloizou 2004). In a disk of particles, the smaller viscosity leads to a smaller type II rate (Ida et al. 2000; Cionco & Brunini 2002; Kirsh et al. 2009; Bromley & Kenyon 2011b). For a circumbinary disk in Pluto–Charon, the expected migration rate is (Bromley & Kenyon 2013)

$$\dot{a}_{II} \approx -0.15 \left( \frac{M_d}{10^{20} \text{ g}} \right) \left( \frac{R}{20 \text{ km}} \right) \left( \frac{a}{20 R_P} \right)^{1/2} \text{ km yr}^{-1}. \quad (33)$$

Satellites migrate more rapidly (i) when the disk is more massive, (ii) when the satellite is more massive, and (iii) when the satellite is closer to the central binary. For standard disk and satellite masses, the Pluto–Charon satellites migrate roughly 1  $R_P$  every  $10^3$  yr.

The ability of satellites to migrate efficiently depends on the ratio of the vertical scale height  $H_z$  to the Hill radius  $R_H$ . When collisional damping dominates particle stirring,  $H_z/R_H \lesssim 1$ . Satellites can open gaps in the disk and migrate at the nominal rates. In a disk dominated by particle stirring,  $H_z/R_H \approx 3(a/20R_P)^{1/2}$  (see eqs. [26–27]). When  $H_z/R_H \gtrsim 1$ , satellites cannot open gaps in the disk. Migration is then ‘attenuated,’ with a rate smaller by a factor of roughly  $(H_z/R_H)^3 \approx 30$ –100 at  $a \approx 20$ –60  $R_P$  (Ida et al. 2000; Kirsh et al. 2009; Bromley & Kenyon 2011b). Despite this reduction, the attenuated type

II rate is still substantial,  $\sim 1 R_P$  every 10 Myr, similar to the time scale for tides and dynamical interactions to modify the semimajor axis of the binary orbit.

This discussion suggests two plausible phases for migration in a circumplanetary disk surrounding Pluto–Charon. During the early stages of the evolution, rapid migration of small satellites is possible when collisional damping dominates particle stirring. Later on, when stirring by newly-formed satellites dominates collisional damping, attenuated migration can modify satellite orbits as the inner binary expands.

## 2.7. Summary of the Physical Model

Our estimates suggest that satellite growth and migration are likely within a circumbinary debris disk produced from material (i) accreted from the protoplanetary disk or (ii) surviving the Pluto–Charon giant impact. If the disk is massive enough, satellite formation in captured material is straightforward: collisional damping produces a disk where small particles can grow into satellites. In debris from a giant impact, material surrounding a Pluto–Charon binary with an initial semimajor axis  $a_{PC} = 5R_P$  (see also Table 2) follows the following evolutionary scenario.

- The impact produces the Pluto–Charon binary with debris along Charon’s orbit (Canup 2011). Charon either accretes or ejects the debris on a time scale  $t \approx 1\text{--}3$  d.
- Particles that survive accretion/ejection lie within a circumbinary ring with semimajor axis  $a_d \approx 20R_P$ . As they make their way into the ring, all debris particles suffer several destructive collisions. Because they are so rare, larger particles might escape the binary more or less intact.
- Shortly after the ring forms, the time scale for viscous spreading is roughly 10 yr. Thus, the ring spreads into a disk.
- Once the disk has  $\delta a/a \approx 1$ , collisional damping promotes the growth of larger objects within the spreading disk. Material from the protoplanetary debris disk adds material to the disk, enhancing the growth rate.
- When particles have sizes of a few km, they migrate through the leftover smaller particles. Although longer than the growth rate, the migration rate is sufficient to transport large objects throughout the circumbinary disk in less than 0.1 Myr.

### 3. NUMERICAL CALCULATIONS OF SATELLITE FORMATION IN THE PARTICLE DISK

Although we cannot perform a complete numerical calculation of satellite formation following a giant impact, we can divide the problem into several pieces which illustrate the likely outcomes. After considering the viscous evolution of a circumbinary disk of particles, we examine the growth and the migration of satellites within this disk (see also Table 2).

To perform these calculations, we use *Orchestra*, an ensemble of computer codes for the formation and evolution of planetary systems. Currently, *Orchestra* consists of a radial diffusion code which computes the time evolution of a gaseous or particulate disk (Bromley & Kenyon 2011a), a multiannulus coagulation code which computes the time evolution of a swarm of planetesimals (Kenyon & Bromley 2004a, 2008), and an  $n$ -body code which computes the orbits of gravitationally interacting protoplanets (Bromley & Kenyon 2006, 2011a). Within the coagulation code, *Orchestra* includes algorithms for treating interactions between small particles and the gaseous disk (e.g., Adachi et al. 1976; Weidenschilling 1977a) and between coagulation mass bins and  $n$ -bodies (Bromley & Kenyon 2006). To treat interactions between small particles and the  $n$ -bodies more rigorously, the  $n$ -body calculations include tracer particles. Massless tracer particles allow us to calculate the evolution of the orbits of small particles in response to the motions of massive protoplanets. Massive tracer particles enable calculations of the response of  $n$ -bodies to the changing gravitational potential of small particles (Bromley & Kenyon 2011a,b, 2013).

#### 3.1. Viscous Evolution

We begin our set of numerical calculations with the evolution of rings of solid particles orbiting a proto-Pluto or the Pluto–Charon binary. The ring has initial mass  $M_d$ , semimajor axis  $a_d$ , and width  $\delta a_d$ . To explore a broad range of plausible initial conditions, we first consider the evolution of a ring of particles orbiting a central object with the mass of Pluto. Next, we examine the evolution around a central mass equivalent to the Pluto–Charon binary. Although not precisely equivalent to a ring orbiting an eccentric binary, these calculations show how different initial conditions change the global evolution of the ring.

### 3.1.1. Diffusion Calculations

To follow the evolution of the surface density of a ring surrounding a planet, we solve the radial diffusion equation (e.g., Lynden-Bell & Pringle 1974; Pringle 1981, 1991),

$$\frac{\partial \Sigma}{\partial t} = 3a^{-1} \frac{\partial}{\partial a} \left( a^{1/2} \frac{\partial}{\partial a} \{ \nu \Sigma a^{1/2} \} \right) - \left( \frac{\partial \Sigma}{\partial t} \right)_{ext}, \quad (34)$$

where  $a$  is the radial distance from the central star and  $t$  is the time. The first term represents the change in surface density  $\Sigma$  from viscous evolution; the second term allows changes in  $\Sigma$  from external processes, including material added from the protoplanetary debris disk.

To derive the appropriate viscosity for the disk, we follow Salmon et al. (2010) and ignore the gravitational scattering component of the viscosity. Although scattering dominates when disk particles are in equilibrium (e.g., eqs. (19–20); see also Shu & Stewart 1985; Hornung et al. 1985), collisions dominate the viscosity during the early stages of the evolution. Thus, our approach yields a good estimate for the viscous time early on, at the expense of a factor of 2–3 underestimate at late times. For this initial exploration of disk evolution in Pluto–Charon, this accuracy is acceptable.

When the disk is gravitationally stable, there are two sources of viscosity from collisions: random motions of particles within the disk ( $\nu_t$ ) and sound waves traveling between colliding particles ( $\nu_c$ ). When the self-gravity of the disk exceeds the rotational shear and the internal velocity dispersion, self-gravity adds another component ( $\nu_g$ ). Self-gravity is important when  $Q_T \lesssim 1$ –2, where

$$Q_T \approx \frac{\Omega v_r}{3.36 G \Sigma} \quad (35)$$

and  $G$  is the gravitational constant (Toomre 1964; Goldreich & Lynden-Bell 1965). The collisional viscosity is independent of  $Q_T$  (Araki & Tremaine 1986):

$$\nu_c = R^2 \Omega \tau. \quad (36)$$

For icy particles with  $\rho = 1 \text{ g cm}^{-3}$ ,  $\tau = 3\Sigma/4R$ . Thus,  $\nu_c$  grows linearly with the particle size and the surface density. The viscosity drops with increasing distance from the central object. The translational viscosity depends on the Toomre stability parameter  $Q_T$  (e.g., Daisaka et al. 2001):

$$\nu_t = \begin{cases} 13 \frac{G^2 \Sigma^2}{\Omega^3} r_h^5 & Q_T < 2 \\ \frac{v_z^2}{\Omega} \left( \frac{0.46 \tau}{1 + \tau^2} \right) & Q_T \geq 2 \end{cases} \quad (37)$$

where  $r_h$  is the ratio of the Hill radius to the radius of a pair of identical particles,  $r_h = R_H/2R$ . The self-gravity component of the viscosity is

$$\nu_g = \begin{cases} \nu_t & Q_T < 2 \\ 0 & Q_T \geq 2 \end{cases} \quad (38)$$

From §2.2, the mass input to the disk is

$$\left(\frac{\partial \Sigma}{\partial t}\right)_{ext} = 3\Sigma_{\odot}\Omega_{\odot}(f\tau_p - \tau_d), \quad (39)$$

where  $f \approx 10^{-3}$  (§2.2);  $\tau_p$  (eq. [5]) and  $\tau_d$  (eq. [7]) are the optical depths of the protoplanetary and circumplanetary disks.

To solve eq. (34), we substitute  $x = 2a^{1/2}$  and  $S = x\Sigma$ . On a grid with 1001 grid points uniformly spaced in  $x$  from the surface of Pluto to  $0.4R_H$ , we use a standard explicit method to derive the evolution of  $S$  with time (e.g., Bath & Pringle 1981; Press et al. 1992). Calculations with a fully implicit approach yield identical results. For explicit and implicit approaches, the calculations conserve mass and angular momentum exactly. For disks surrounding single and binary planets, we adopt a flow through outer boundary condition, with  $\Sigma = 0$  at  $a = 0.4R_H$ . For a single planet, we adopt the flow through boundary condition at the planet’s surface,  $a = R_P$ . To treat truncation of the disk by the inner binary, we follow Pringle (1991) and set the radial velocity of disk material at this boundary to zero. Formally, the boundary condition is

$$\frac{\partial}{\partial x}(\nu\Sigma x) = 0. \quad (40)$$

We apply this boundary condition at  $a = a_{min}$  (eq. [10]).

### 3.1.2. Before Impact: Circumplanetary Disk Evolution

To explore whether circumplanetary disks have sufficient mass to produce the satellites orbiting Pluto–Charon, we consider the evolution of a low mass ring surrounding a Pluto-mass protoplanet. As a standard model, we adopt small particle sizes,  $10^3$  cm, for material in the circumplanetary disk, which implies a small radial velocity dispersion,  $0.5$  cm s $^{-1}$ . The calculation begins with a low mass ( $M_d = 10^{11}$  g) ring at  $a = 20R_P$ . To derive the maximum disk mass, material is added at the rate from eq. (39) with a depletion factor  $f_{\odot} = 1$ .

Fig. 3 illustrates the long-term growth of the circumplanetary disk. New material from the protoplanetary disk gradually erases the initial conditions and produces a roughly constant surface density from the surface of the proto-planet to the edge of the stable region at  $0.4 R_H$ . As the system evolves, the surface density slowly increases. After an evolution time of 100 Myr, the system begins to reach a steady-state with a total disk mass of  $M_{d,ss} \approx 2.5 \times 10^{19}$  g. Although the steady-state surface density distribution peaks close to the central proto-planet, the distribution is shallow, with  $\Sigma \propto a^{-n}$  and  $n \approx 0.20$ - $0.25$ .



The behavior of the surface density in Fig. 3 has two main causes. Early on, the disk has little mass and very low optical depth. Material from the protoplanetary disk rarely interacts with the circumplanetary disk. Thus, there is little collisional depletion. During this period, the surface density remains roughly constant with radius. As the evolution proceeds, the disk optical depth grows, eventually enabling collisions with disk material. Because the disk has a larger scale height at the outer edge of the disk, there is relatively more depletion from the outer disk than the inner disk. This extra depletion produces a maximum surface density close to the central planet.

Throughout the evolution, the disk transfers material inwards onto the central planet and outwards into the protoplanetary disk. After  $\sim 1$  Gyr, the planet accretes a negligible amount of material,  $\sim 10^{12}$  g. Because most disk material is added near the outer radius, the disk transports a much larger amount of material into the protoplanetary disk,  $\sim 10^{14}$  g. This material makes a negligible contribution to the  $\sim 10^{25}$  g orbiting within 5–10 Hill radii of the planet. Thus, material from the circumplanetary disk has a limited impact on the mass of the central planet or the evolution of the protoplanetary debris disk.

The mass of the steady-state circumplanetary disk scales with the adopted accretion efficiency  $f$ , the depletion of the protoplanetary disk  $f_{\odot}$ , and the radius of a typical large object in the protoplanetary disk  $R_{max}$ . The numerical results are close to the analytic estimate in §2.2:

$$M_{d,ss} \approx 2.5 \times 10^{19} f_{\odot} \left( \frac{f}{10^{-3}} \right) \left( \frac{R_{max}}{100 \text{ km}} \right)^{-1} \left( \frac{a_{\odot}}{20 \text{ AU}} \right)^{3/2}. \quad (41)$$

Although the steady-state disk mass is independent of the particle size in the disk, the amount of material accreted by the central planet and the amount transported out through the disk vary with particle size. In the outer disk, larger viscosity enables more mass transport. Thus, mass loss through the outer edge of the disk grows roughly linearly with the particle size. In the inner disk, mass accretion depends on the viscosity and on the rate angular momentum flows out through the disk. Larger viscosity increases the efficiency of both processes. Thus, the mass accretion rate grows somewhat less rapidly with particle size. In all cases, the total mass accreted onto the planet or lost into the protoplanetary disk is smaller than the steady-state mass in the disk.

### 3.1.3. *After Impact: Circumbinary Disk Evolution*

We now consider the viscous evolution of a circumbinary ring of material formed during the Pluto–Charon giant impact. The calculations assume a narrow ring of solid particles with

total mass  $M_d$  at initial semimajor axis  $a = 20 R_P$ . The particles have radius  $R = 0.1$  km and radial velocity dispersions  $v_r = 5, 50, \text{ or } 500 \text{ cm s}^{-1}$ . In the first set of calculations, the Pluto–Charon binary has fixed separation  $a_{PC} = 5 R_P$ . In the second set of calculations, the binary expands from an initial  $a_{PC} = 5 R_P$  to the current  $a_{PC} = 17 R_P$  over several Myr (eq. [16]).

Fig. 4 shows results for calculations with  $M_d = 3 \times 10^{20}$  g. Initially, the solids lie in a narrow annulus at  $a = 20R_P$ , roughly half the semimajor axis of the current satellites. At the start of the calculation, the ring spreads roughly uniformly inward and outward. Eventually, the inner edge of the disk reaches a semimajor axis  $a_{min} = 2a_{PC}$ . The inner boundary condition prevents material from flowing in past this semimajor axis. The inner edge then remains fixed while the outer radius spreads outward.

At all times, the extent of the disk depends on the radius and the radial velocity dispersion of the solids (Fig. 4). In disks with  $R = 0.1$  km and  $v_r = 5 \text{ cm s}^{-1}$  (blue curves), viscous spreading is slow. It takes roughly 1 Myr for the inner edge of the disk to reach  $a = 2a_{PC}$  and more than 10 Myr for the outer edge of the disk to reach the current orbits of the small Pluto–Charon satellites,  $a \approx 40 - 60R_P$ . Disks with larger velocity dispersions evolve more rapidly. When  $v_r = 500 \text{ cm s}^{-1}$  (maroon curves), the inner edge of the disk reaches  $a \approx 2a_{PC}$  in only  $10^3$  yr. At  $\sim 10^4$  yr, the outer edge of the disk crosses the orbits of P5, Nix, P4, and Hydra.

Far away from the inner and outer edges, the surface density follows a power law with  $\Sigma \propto a^{-n}$ . During the early stages of the evolution, the power law is steep, with  $n \approx 2$ . As the evolution proceeds, the surface density distribution becomes shallower, with  $n \approx 1.0\text{--}1.5$ . After roughly 1 Gyr, the outer edge of the disk reaches  $a \approx 0.4R_H$ . The slope is then very shallow, with  $n \approx 0.5\text{--}1.0$ .

When we include the tidal expansion of the binary orbit, the evolution of the solids changes dramatically (Fig. 5). As the binary expands, the inner boundary condition maintains the inner edge of the disk at  $a = 2a_{PC}$ . Thus, the inner disk expands in step with the binary orbit. Throughout the disk, the viscosity is independent of the inner boundary condition. The expanding binary has little impact on the evolution of the outer edge of the disk. With a larger inner disk radius and a similar outer disk radius, the disk covers a much smaller radial extent compared to calculations without an expanding inner binary.

Despite differences in the radial extent of the disk, the evolution of the slope of the surface density distribution is fairly independent of the evolution of the central binary. Early on,  $\Sigma \propto a^{-n}$  with  $n \approx 2$ . As the binary approaches its current separation of  $17 R_P$ , the slope slowly declines to  $n \approx 1.0\text{--}1.5$ . At very late times,  $\sim 100$  Myr to 1 Gyr, the slope is

shallower still, with  $n \approx 0.5\text{--}1.0$ .

Calculations with different combinations of disk mass, particle size, and radial velocity dispersion lead to similar results. The time scale for the outer edge of the disk to reach the current orbits of the satellites depends on the initial mass in the debris, the typical radius of particles in the disk, and the radial velocity dispersion of disk particles. For our calculations, the time scale for outer disk material to reach  $a = 50 R_P$  is

$$t_{50} \approx 1 \left( \frac{10^{22} \text{ g}}{M_d} \right) \left( \frac{R_{max}}{1 \text{ km}} \right) \left( \frac{50 \text{ cm s}^{-1}}{v_r} \right)^2 \text{ Myr} . \quad (42)$$

Massive disks composed of small particles with large velocity dispersions evolve on the fastest time scales.

The scaling in eq. (42) depends solely on the translational viscosity  $\nu_t$ . For  $M_d \approx 10^{18} - 10^{22}$  g,  $\nu_t$  contributes more to the viscosity than  $\nu_c$  (see eqs. [36]–[37]). Because  $\nu_t \propto \Sigma v_r^2 R^{-1}$ , the viscosity grows linearly with increasing disk mass, falls linearly with increasing particle size, and grows with the square of the radial velocity dispersion. Thus, the viscous time scale  $t_\nu \propto R M_d^{-1} v_r^{-2}$ .

For the satellites orbiting Pluto–Charon, these results have several clear consequences.

- Because the disk and the inner binary expand at comparable rates, understanding the origin of the 3:4:5:6 period ratio for the satellites requires treating the evolution of the central binary and the disk of debris simultaneously (see also Ward & Canup 2006; Lithwick & Wu 2008).
- In §2, our results suggest that debris ejected from the vicinity of the Pluto–Charon binary probably consists of many small particles with  $R \lesssim 0.1$  km and perhaps a few large objects,  $R \approx 10\text{--}20$  km, which do not suffer destructive collisions during the ejection process. The diffusion calculations indicate that debris with a few large objects – and hence large velocity dispersions – evolves more rapidly than debris with no large objects. Thus, understanding the details of satellite formation requires better knowledge of the evolution of debris during the impact.
- Disks with smaller radial velocity dispersions are narrower in semimajor axis than disks with larger radial velocity dispersions. If migration is unimportant, the current orbits of P5, Nix, P4, and Hydra are easier to understand if the initial velocity dispersion of the debris is small. Rapid migration allows a broader range of initial velocity dispersions. We return to this point in §3.3.

- Disks with smaller radial velocity dispersion expand out to the current orbits of P5, Nix, P4, and Hydra on much longer time scales than disks with larger radial velocity dispersion. If satellites form rapidly, on time scales less than  $10^4 - 10^5$  yr, the orbits of the satellites depend on how they respond to the expansion of the inner binary and the expansion of the disk. If the satellites form on 1–10 Myr, interactions with the remnant disk are more important than interactions with the central binary. We consider the formation time in §3.2.

#### 3.1.4. Summary of Viscous Disk Calculations

The results of the diffusion calculations show that the satellites orbiting the Pluto–Charon binary are somewhat more likely to form in the debris from the giant impact than in material accreted from the protostellar disk. Unless accretion from the protostellar disk is more efficient than our estimates suggest, the mass of a circumplanetary disk surrounding a proto-Pluto is a factor of 1.5–10 times smaller than the current mass of the satellites. The amount of debris produced in a giant impact is uncertain by a factor of 10–100 (Canup 2011). Some impacts yield masses large enough to produce P5, Nix, P4, and Hydra.

Although debris from the impact initially lies well inside the current orbits of the satellites, viscous diffusion and tidal evolution of the Pluto–Charon binary drive disk material to larger orbits on interesting time scales. Expansion of the binary prevents disk material from spreading inside  $a \approx 2a_{PC}$ . Once Charon achieves its current orbit with  $a_{PC} = 17 R_P$ , disk material orbits outside  $a \approx 34R_P$ . Thus, the dynamics of the binary orbit precludes satellites inside the orbit of P5. Viscous spreading transports disk material to large radii,  $a \gtrsim 60R_P$ , in roughly 1 Myr. Because a broad range of  $M_d$ ,  $R$ , and  $v_r$  yield disk material at the current orbits of the four satellites, the satellites could plausibly form within a variety of disks.

To place additional constraints on satellite production, we now examine the growth of satellites in a disk of particles.

### 3.2. Growth of Satellites in the Particle Disk

To calculate the growth and evolution of satellites in a disk of small particles, we use a hybrid multiannulus coagulation– $N$ -body code. We compute the collisional evolution of an ensemble of particles in a disk orbiting a central object of mass  $M_{PC}$ . The code uses statistical algorithms to evolve the mass and velocity distributions of low mass objects with

time and an  $N$ -body algorithm to follow the individual trajectories of massive objects. Kenyon & Bromley (2008) describe the statistical (coagulation) code; Bromley & Kenyon (2006, 2011a) describe the  $N$ -body code. Here, we briefly summarize the basic aspects of our approach (for a general review of collisional evolution, see Youdin & Kenyon 2012).

We perform calculations on a cylindrical grid with inner radius  $a_{in}$  and outer radius  $a_{out}$ . The model grid contains  $N$  concentric annuli with widths  $\delta a_i = 0.025a_i$  centered at semimajor axes  $a_i$ . Calculations begin with a cumulative mass distribution  $n_c(m_{ik}) \propto m_{ik}^{-q'}$  of particles with mass density  $\rho = 1 \text{ g cm}^{-3}$  and maximum initial mass  $m_0$ . For comparison with investigators that quote differential size distributions with  $n \propto r^{-q}$ ,  $q' = q + 1$ . Here, we adopt an initial  $q'_0 = 0.17$ ; thus most of the initial mass is in the largest objects.

Planetesimals have horizontal and vertical velocities  $h_{ik}(t)$  and  $v_{ik}(t)$  relative to a circular orbit. The horizontal velocity is related to the orbital eccentricity,  $e_{ik}^2(t) = 1.6 (h_{ik}(t)/V_{K,i})^2$ , where  $V_{K,i}$  is the circular orbital velocity in annulus  $i$ . The orbital inclination depends on the vertical velocity,  $i_{ik}^2(t) = \sin^{-2}(2(v_{ik}(t)/V_{K,i}))$ .

The mass and velocity distributions of the planetesimals evolve in time due to inelastic collisions, drag forces, and gravitational encounters. As summarized in Kenyon & Bromley (2004a, 2008), we solve a coupled set of coagulation equations which treats the outcomes of mutual collisions between all particles with mass  $m_j$  in annuli  $a_i$ . We adopt the particle-in-a-box algorithm, where the physical collision rate is  $n\sigma v f_g$ ,  $n$  is the number density of objects,  $\sigma$  is the geometric cross-section,  $v$  is the relative velocity, and  $f_g$  is the gravitational focusing factor. Depending on physical conditions in the disk, we derive  $f_g$  in the dispersion or the shear regime (Kenyon & Bromley 2012). For a specific mass bin, the solutions include terms for (i) loss of mass from mergers with other objects and (ii) gain of mass from collisional debris and mergers of smaller objects.

Collision outcomes depend on the ratio  $Q_c/Q_D^*$ , where  $Q_D^*$  is the collision energy needed to eject half the mass of a pair of colliding planetesimals to infinity and  $Q_c$  is the center of mass collision energy. To derive  $Q_D^*$  (eq. [2]), we adopt parameters for weak particles (Table 3). For two colliding planetesimals with masses  $m_1$  and  $m_2$ , the mass of the merged planetesimal is

$$m = m_1 + m_2 - m_{ej} , \quad (43)$$

where the mass of debris ejected in a collision is

$$m_{ej} = 0.5 (m_1 + m_2) \left( \frac{Q_c}{Q_D^*} \right)^{9/8} . \quad (44)$$

To place the debris in our grid of mass bins, we set the mass of the largest collision fragment as  $m_L = 0.2m_{esc}$  and adopt a cumulative mass distribution  $n_c \propto m^{-q_d}$  with  $q_d =$

0.833, roughly the value expected for a system in collisional equilibrium (Dohnanyi 1969; Williams & Wetherill 1994; Tanaka & Ida 1996; O’Brien & Greenberg 2003; Kobayashi & Tanaka 2010). This approach allows us to derive ejected masses for catastrophic collisions with  $Q_c \sim Q_D^*$  and for cratering collisions with  $Q_c \ll Q_D^*$  (see also Wetherill & Stewart 1993; Williams & Wetherill 1994; Tanaka & Ida 1996; Stern & Colwell 1997; Kenyon & Luu 1999; O’Brien & Greenberg 2003; Kobayashi & Tanaka 2010).

To compute the evolution of the velocity distribution, we include collisional damping from inelastic collisions and gravitational interactions. For inelastic and elastic collisions, we follow the statistical, Fokker-Planck approaches of Ohtsuki (1992) and Ohtsuki et al. (2002), which treat pairwise interactions (e.g., dynamical friction and viscous stirring) between all objects in all annuli. As in Kenyon & Bromley (2001), we add terms to treat the probability that objects in annulus  $i_1$  interact with objects in annulus  $i_2$  (Kenyon & Bromley 2004a, 2008). We also compute long-range stirring from distant oligarchs (Weidenschilling 1989).

In the  $N$ -body code, we directly integrate the orbits of objects with masses larger than a pre-set ‘promotion mass’  $m_{pro}$ . The calculations allow for mergers among the  $N$ -bodies. Additional algorithms treat mass accretion from the coagulation grid and mutual gravitational stirring of  $n$ -bodies and mass batches in the coagulation grid. To treat interactions among proto-satellites, we set  $m_{pro} = 10^{17} - 10^{19}$  g.

Our calculations follow the time evolution of the mass and velocity distributions of objects with a range of radii,  $r_{ij} = r_{min}$  to  $r_{ij} = r_{max}$ . To track the amount of material ejected by radiation pressure, we set  $r_{min} = 20 \mu\text{m}$ . The upper limit  $r_{max}$  is always larger than the largest object in each annulus.

### 3.2.1. Pure Coagulation Calculations

To explore possible outcomes for an ensemble of solid particles orbiting the Pluto–Charon binary, we consider a suite of pure coagulation calculations. The calculations begin with a ring of material surrounding a central mass equivalent to the Pluto–Charon binary. The total mass in the ring ranges between  $M_d = 3 \times 10^{19}$  g and  $M_d = 3 \times 10^{21}$  g. The ring consists of 32 concentric, circular annuli extending from  $15 R_P$  to  $50 R_P$ . This cylindrical grid provides a reasonably accurate representation of orbits of debris particles from the giant impact around a circular binary system with an initial separation of  $5 R_P$ .

Debris captured from the protoplanetary disk lies at much larger disk radii than considered in these calculations. Because coagulation calculations are easily scaled to different semimajor axes (Kenyon & Bromley 2008, 2010), it is straightforward to apply our results

to the larger disks produced by capture.

Within each annulus, the solid particles range in size from  $20 \mu\text{m}$  to  $0.1 \text{ km}$ . Consistent with solutions for the radial diffusion equation in §3.1, the initial surface density distribution is  $\Sigma \propto a^{-1}$ . To allow the system to find an equilibrium between the large orbital eccentricity of material ejected from the central binary and the small eccentricity expected from collisional damping, we adopt an initial eccentricity  $e_0 = 0.1$  and an initial inclination  $i_0/e_0 = 0.5$ .

All of these calculations follow a similar pattern. With the large initial  $(e, i)$  of all particles, collisions among large particles are destructive and produce copious amounts of smaller particles. Among the smaller particles, collisional damping is effective. Through dynamical friction, smaller particles damp the orbits of the larger particles. Thus, the  $(e, i)$  for all particles declines with time. Collisions become less destructive. Eventually, collisional velocities become small enough to promote growth over destruction. During this phase, roughly 25% of the initial mass is ground down into particles smaller than  $20 \mu\text{m}$ . This material is ejected from the binary.

After the system reaches a low velocity equilibrium, the largest particles begin to grow rapidly. During a very short phase of runaway growth, objects grow from roughly  $0.1 \text{ km}$  to  $3\text{--}30 \text{ km}$ . As the largest objects grow, they gravitationally stir the smaller particles. Once the largest objects contain most of the mass, stirring dominates collisional damping. The orbital  $(e, i)$  of the smaller objects rapidly increases, reducing gravitational focusing factors and halting runaway growth. At the end of runaway growth, each annulus contains a handful of proto-satellites with radii of  $3\text{--}30 \text{ km}$ .

Following runaway growth, the evolution of the system stalls. The proto-satellites rapidly accrete any small particles left in their annuli. Because the small particles contain so little mass, this growth of the large particles is very small. In the particle-in-a-box approximation adopted for these pure coagulation calculations, the probability of collisions among large objects is small. Thus, the sizes of the proto-satellites reach a rough steady state set approximately by the initial mass in each annulus of the grid.

Figure 6 illustrates the growth of satellites for calculations with  $M_d = 3 \times 10^{19} \text{ g}$  (thin lines) and  $M_d = 3 \times 10^{21} \text{ g}$  (thick lines). As summarized in the caption, each line represents the evolution in the radius of the largest object in annuli ranging in distance from  $15 R_P$  to  $50 R_P$  from the center-of-mass. In these disks, satellite growth is very rapid. Despite an initial period of destructive collisions, it takes only  $1\text{--}100 \text{ yr}$  for an ensemble of  $0.1 \text{ km}$  fragments to grow into  $10 \text{ km}$  satellites. The growth time is inversely proportional to the initial disk mass,  $t_g \approx 100(3 \times 10^{20} \text{ g}/M_d) \text{ yr}$ . Once satellites reach a maximum mass of  $5\text{--}50 \text{ km}$ , growth stalls. Satellites remain at a roughly constant radius for thousands of

years.

These calculations demonstrate the inevitable growth of 5–30 km satellites from an ensemble of much smaller objects. Independent of the initial orbital eccentricity, collisional damping reduces the internal velocity dispersion to levels that promote mergers during collisions. Despite the loss of roughly 25% of the initial mass to a collisional cascade, small objects grow rapidly into satellites with radii of 5–30 km. The growth time is short compared to the time scale for viscous spreading of the disk (Fig. 5) or the time scale for binary expansion (eq. [16]). Thus, the growth of small satellites orbiting the Pluto–Charon binary is very efficient.

Despite the efficiency of small satellite formation, coagulation calculations produce too many satellites. In these models, each of the 32 annuli in the calculation yields 0–3 satellites with radii of 5–30 km. Even with small number statistics, this result is much larger than the current number of known satellites. However, the coagulation calculations do not allow large-scale dynamical interactions among satellites. For the models shown in Fig. 6, satellites in adjacent annuli have orbital separations of 5–15  $R_P$ . Thus, satellites are close enough to perturb the orbits of their nearest neighbors, leading to chaotic interactions as in simulations of terrestrial planet formation (Kenyon & Bromley 2006).

### 3.2.2. Hybrid Calculations

To investigate dynamical interactions among newly-formed satellites, we now consider a suite of hybrid simulations with *Orchestra*. Objects in the coagulation code which reach a preset mass,  $m_{pro}$ , are promoted into the  $n$ -body code. When a satellite with  $(m_{ij}, e_{ij}, i_{ij})$  in an annulus with semimajor axis  $a_i$  is promoted, we assign  $(e_n, i_n) = (e_{ij}, i_{ij})$ ,  $a_n = a_i + g\Delta a_i$ , and a random orbital phase, where  $g$  is a random number in the range  $-0.5$  to  $+0.5$ . The  $n$ -body code converts these orbital elements into an initial  $(x, y, z)$  position and an initial  $(v_x, v_y, v_z)$  velocity vector. The  $n$ -body code follows the trajectories of all promoted satellites. Algorithms within *Orchestra* allow  $n$ -bodies to interact with coagulation particles (Bromley & Kenyon 2006, 2011a).

The starting conditions for these calculations are identical to those for the pure coagulation models. We consider three cases for the initial disk mass,  $m_d = 3 \times 10^{19}$  g (low mass disk),  $m_d = 3 \times 10^{20}$  g (intermediate mass disk), and  $m_d = 3 \times 10^{21}$  g (massive disk). For each case, we adopt a different promotion mass:  $m_{pro} = 3 \times 10^{17}$  g (low mass),  $m_{pro} = 10^{18}$  g (intermediate mass), and  $m_{pro} = 3 \times 10^{18}$  g (high mass). These promotion masses are a compromise between the ‘optimal’ promotion mass,  $m_{pro} = 3 - 30 \times 10^{16}$  g, required to allow



newly formed  $n$ -bodies to adjust their positions and velocities to existing  $n$ -bodies and the practical limits required to complete calculations in a reasonable amount of time. For each combination of disk mass and promotion mass, we ran 20–25 simulations.

To check the accuracy of our results for the intermediate and high mass disks, we ran an additional 12 simulations for each of two cases with promotion masses a factor of three larger and a factor of three smaller than the promotion masses listed above. When the promotion mass is a factor of three larger, the chaotic growth phase begins later and lasts longer. Often, chaotic growth in the outer disk is (unphysically) well-separated in time from chaotic growth in the inner disk. This feature inhibits scattering and radial mixing among proto-satellites. When the promotion mass is a factor of three smaller, the onset, character, and duration of chaotic growth changes very little. In all cases, the final number of satellites is fairly independent of promotion mass.

Because fragmentation has a small impact on the results of pure coagulation calculations per unit cpu time, these hybrid calculations do not include fragmentation. Neglecting fragmentation increases the mass available for satellite growth by roughly 25%. Without fragmentation, collisions fail to produce copious amounts of 1 m to 100 m particles. Collisional damping among these debris particles and dynamical friction between the debris and larger survivors reduces orbital  $e$  and  $i$ , aiding runaway growth. Thus, these hybrid calculations artificially increase the evolution time required for satellites to reach  $R \gtrsim 10$  km.

Fig. 7 shows the evolution of the semimajor axes for promoted satellites orbiting a single central object with the mass of the Pluto–Charon binary. All objects begin with  $r \lesssim 0.1$  km ( $m \lesssim 4 \times 10^{12}$  g). The evolution time required for these objects to reach the promotion mass scales with the initial disk mass,  $t_{pro} \approx 10^3$  ( $3 \times 10^{19}$  g/ $m_d$ ) yr. This time scale is roughly a factor of ten longer than derived for pure coagulation calculations with fragmentation. In the inner disk, objects have shorter orbital periods and shorter collision times. Thus, the first promoted objects appear near the inner edge of the disk. As the calculation proceeds, satellites are promoted farther and farther out in the disk. Eventually, a few promoted objects appear in the outer disk.

Every calculation experiences chaotic growth (Goldreich et al. 2004; Kenyon & Bromley 2006). During chaotic growth, the satellites scatter one another throughout the grid. Because objects grow fastest in the most massive disks, chaotic growth begins earlier –  $\sim 100$  yr – in the high mass disk and much later –  $\sim 10^4$  yr – in the low mass disk. Chaotic growth is also ‘stronger’ in more massive disks. In more massive disks, massive large satellites are more numerous and generate larger radial excursions of smaller satellites than in lower mass disks.

Throughout the evolution shown in Fig. 7, the  $n$ -bodies slowly accrete the very small planetesimals remaining in the coagulation grid. The number of leftovers correlates well with the number of  $n$ -bodies. Thus, the total mass in leftover planetesimals within the coagulation grid approaches zero as the number of  $n$ -bodies reaches a minimum.

In all of these calculations, the final number of satellites correlates inversely with the initial disk mass. In massive disks with  $M_d = 3 \times 10^{21}$  g, there are usually 2 or 3 massive satellites with  $r \approx 50$ –80 km at the end of the calculation. As we reduce the initial disk mass, the calculations produce more satellites with smaller masses. In intermediate mass disks with  $M_d = 3 \times 10^{20}$  km, chaotic growth leaves all of the initial mass in 4–5 satellites with radii of 20–30 km. In low mass disks, there are very few mergers during chaotic growth. After  $\sim 10^7$  yr, there are typically 7–9 satellites with radii of 7–12 km.

To test how outcomes change with the initial size distribution, we consider a suite of 15 simulations with two additional 10 km planetesimals placed randomly in the grid. These large planetesimals stir their surroundings and thus counteract collisional damping by nearby small planetesimals. With much larger masses than any other planetesimals in the grid, they have large collisional cross-sections and can grow very rapidly.

Fig. 8 compares the time evolution of the semimajor axes for  $n$ -bodies in calculations with (lower panel) and without (upper panel) two additional massive planetesimals. In standard calculations with  $M_d = 3 \times 10^{19}$  g, there is a short period of chaotic growth at  $\sim 10^4$ – $10^5$  yr followed by a long quiescent period with an occasional merger. When there are two large planetesimals at the onset of the calculation, these planetesimals slowly accumulate small planetesimals. Meanwhile, small planetesimals in the rest of the disk rapidly grow into sizes (4–5 km) that allow promotion into the  $n$ -body code. From Fig. 8, the time scale for these objects to reach the promotion mass is roughly  $10^3$  –  $10^4$  yr independent of the two large satellites. However, stirring by the two large satellites promotes an earlier oligarchic growth phase which enables more uniform growth of the largest planetesimals. Thus, there are many more promoted objects and a more intense chaotic growth phase. In addition to the two initial massive planetesimals, one or two other planetesimals accrete all of the other promoted objects. After  $\sim 10^5$  yr, there are only a few small  $n$ -bodies left. The 3–4 massive satellites accrete these objects in a few hundred thousand years.

This result is typical of all calculations in low or intermediate mass disks that begin with a few large (10 km) planetesimals placed randomly throughout the grid. Stirring by the large objects slows runaway growth and allows a larger group of oligarchs to grow rapidly. Although these oligarchs reach the promotion mass on similar time scales, many more of them reach the promotion mass. Typically, calculations with initial large planetesimals produce 2–4 times as many  $n$ -bodies as calculations without large planetesimals. Stirring by the

10 km planetesimals and interactions among the many  $n$ -bodies leads to a very active phase of chaotic growth. During chaotic growth, the radial excursions of the  $n$ -bodies are 2–3 times larger in semimajor axis. Collisions among  $n$ -bodies are more frequent, leading to a system with fewer, but more massive, satellites. With a set of two initially large planetesimals, low (intermediate) mass disks produce 3–4 (2–3) massive satellites instead of 7–9 (4–5).

For all of these hybrid calculations, the radius evolution follows a standard pattern (Fig. 9). As in Fig. 6, the largest objects in the coagulation grid grow from 0.1 km to 1–10 km. Once they are promoted into the  $n$ -body grid, they interact with objects in the coagulation grid *and* all of the promoted objects in the  $n$ -body grid. Unlike the pure coagulation calculations, growth does not stall at 5–30 km. The extra interactions between promoted objects and the larger volume sampled by scattered objects enables a few large objects to accumulate all of the remaining mass in the grid. Thus, these objects reach radii that are 30% to 100% larger (and 2–8 times more massive) than the largest objects in the pure coagulation calculations.

To conclude this section, Fig. 10 plots pairs of  $(e, i)$  for satellites that survive for  $10^7$  yr. For most satellites, the orbital inclination is small: the average inclination is  $\langle i \rangle = 0.1^\circ \pm 0.2^\circ$ . Despite the apparent excess of high  $i$  objects at small  $e$  for the low and intermediate mass disks, the average  $i$  and the dispersion in the average do not vary with initial disk mass. The average  $e$  grows with disk mass, however, with  $\langle e \rangle = 0.02 \pm 0.02$  for  $M_d = 3 \times 10^{19}$  g,  $\langle e \rangle = 0.03 \pm 0.02$  for  $M_d = 3 \times 10^{20}$  g, and  $\langle e \rangle = 0.06 \pm 0.06$  for  $M_d = 3 \times 10^{21}$  g. For small and intermediate initial disk masses, the average eccentricity is very low. For large disk masses, the  $\langle e \rangle$  is a factor of 2–3 larger.

Although the final orbital elements of satellites are independent of the promotion mass,  $e$  depends on the initial masses of the largest planetesimals. When we add several large planetesimals to the initial distribution of 0.1 km and smaller planetesimals, the calculations yield fewer satellites with larger masses (Fig. 8). As in calculations with larger total disk masses, a few large satellites stir up their surroundings more than many smaller satellites. These satellites then have larger  $e$ .

### 3.2.3. *Summary of Coagulation and Hybrid Calculations*

The suite of pure coagulation and hybrid calculations demonstrates that the Pluto–Charon satellites grow rapidly from a disk of small planetesimals. When calculations include fragmentation, destructive collisions grind down roughly 25% of the initial disk mass into 20  $\mu\text{m}$  particles which are ejected from the binary system. Collisional damping among

larger debris particles reduces orbital eccentricity of 0.1–10 m objects. Dynamical friction between these small planetesimals and the surviving large planetesimals damps the orbital eccentricities of the largest objects, greatly reducing the frequency of destructive collisions and enabling rapid growth of surviving planetesimals. Thus, fragmentation removes mass and aids the eventual rapid growth of satellites.

In hybrid calculations without fragmentation, less collisional damping and dynamical friction slow growth considerably. However, satellites still grow on time scales similar to the expansion time for the central binary. The number of satellites  $N_s$ , typical satellite radius  $R_s$ , and the time for satellites to reach their final mass  $t_f$  scales with the initial mass of the planetesimal disk. For calculations without any large (10 km) fragments at  $t = 0$  and  $M_d \approx 3 - 300 \times 10^{19}$  g, we infer

$$N_s \approx 2^{22.5 - \log M_d} , \quad (45)$$

for the number of satellites

$$R_s \approx 27.5 \left( \frac{3 \times 10^{20} \text{ g}}{M_d} \right)^{0.425} \text{ km} , \quad (46)$$

for the typical radius, and

$$t_f \approx 10^4 \left( \frac{3 \times 10^{21} \text{ g}}{M_d} \right) \text{ yr} . \quad (47)$$

for the growth time.

In low and intermediate mass disks, calculations with several 10 km fragments produce fewer satellites with larger masses. For  $M_d \approx 3 - 30 \times 10^{19}$  g,  $N_s \approx 3-5$  and  $R_s \approx 15-60$  km instead of the  $N_s \approx 4-10$  and  $R_s \approx 7-30$  km for calculations without large fragments. Because large fragments tend to sweep up any small planetesimals, calculations with fragments yield a smaller spread in the number and masses of planetesimals than calculations without fragments.

The orbital elements of model satellites agree reasonably well with the observed elements of the Pluto–Charon satellites. Roughly 10% of the model satellites have  $e \lesssim e_H$ , where  $e_H$  is the orbital eccentricity of Hydra. Nearly all (83%) satellites have orbital inclinations  $i \lesssim i_H$ , where  $i_H$  is the inclination of Hydra. Satellites with integer period ratios are also common. For calculations with  $M_d = 3 \times 10^{21}$  g, 60% of the outer satellites have period ratios reasonably close to the 5:3, 2:1, or 3:1 commensurabilities with the inner satellite. Disks with smaller initial masses produce more closely-packed, lower mass satellites which often lie close to the 3:2 and 4:3 commensurabilities. For these lower mass disks, 50% to 70% of satellites have period ratios within a few per cent of the 4:3, 3:2, 5:3, 2:1, or 3:1 commensurabilities.

These results are encouraging. Model satellites often lie close to the observed orbital commensurabilities in the Pluto–Charon satellites. The derived inclinations of model satellites also agree very well with observations. Although lower mass disks produce satellites with the smallest  $e$ , derived eccentricities for all calculations are factor of 4–20 larger than observed. Thus, the calculations have two successes – the small inclinations and the likelihood of close orbital commensurabilities – and one failure – the lack of very small eccentricities for the satellites.

To explore the outcomes of formation models in more detail, we now consider numerical calculations of satellite migration through the circumbinary disk surrounding Pluto–Charon. Aside from testing the analytic estimates for  $R_{gap}$ ,  $R_{fast}$ , and  $\dot{a}$  from §2.5, these calculations allow us to estimate the frequency of migration-driven mergers and to examine the evolution of  $e$  and  $i$  for an ensemble of migrating satellites.

### 3.3. Migration of Satellites Through the Circumbinary Disk

To explore satellite migration, we use the  $N$ -body component of the *Orchestra* code. In this mode, the calculations directly track interactions between satellites and massive “super-particles” that represent small particles in the disk. For massive objects within a disk around a single central object, our calculations (Bromley & Kenyon 2011a,b) reproduce published results of previous investigators (e.g., Malhotra 1993; Hahn & Malhotra 1999; Kirsh et al. 2009). Our investigation of migration within Saturn’s rings includes extensive tests with gaps in the disk, orbital resonances, and the gravitational perturbations of distant massive moons outside resonance (Bromley & Kenyon 2013). To test the theoretical limits on migration rates in a disk surrounding Pluto–Charon, we first consider calculations of a lone satellite with  $R \approx R_{gap} - R_{fast}$  within a particle disk around a single central object with the combined mass of Pluto–Charon. We then consider how a binary central object modifies the mode and rate of migration. Because the hybrid calculations often produce many small satellites, we conclude this section with simulations of multiple satellites orbiting a central binary.

For this suite of simulations, we adopt a disk surface density distribution,  $\Sigma \propto a^{-1}$ , with a fixed mass of  $3 \times 10^{20}$  g. The disk extends from  $a = 20 R_P$  to  $a = 70 R_P$  around a single object with a radius of  $1 R_P$  or a binary with a separation of  $5 R_P$ . We follow an ensemble of super-particles and satellites in an annulus of full width of  $5 R_P$ . Super-particles have masses of  $1/2000^{\text{th}}$  the mass of the satellite. These objects interact with the satellite and the central mass, but not with each other. Satellites have fixed bulk mass density,  $\rho = 1 \text{ g/cm}^3$ .

At the start of each simulation, super-particles are dynamically cold. Thus, the disk

is geometrically thin, with  $H_z/R_H \lesssim 1$ . Particle trajectories evolve solely by interactions with the central (single or binary) object and massive satellites. Unlike our simulations of Saturn’s A ring (Bromley & Kenyon 2013), there is no collisional damping among super-particles. These initial conditions are ideal to assess a satellite’s ability to migrate through the disk and lead to fairly robust upper limits on the migration rate. In a more realistic disk, collisional damping, dynamical friction, and viscous stirring generally produce increases in the velocity dispersion and vertical scale height of disk particles on time scales comparable to the growth time (see §3.2). Because migration rates fall off as the inverse cube of the mean disk particle eccentricity (Ida et al. 2000; Kirsh et al. 2009; Bromley & Kenyon 2011b), we expect that migration time scales in a real disk are somewhat longer than our estimates for idealized disks.

### 3.3.1. Migration of a Single Satellite

Figure 11 illustrates results for single satellites around a single central mass (left panels) and a central binary system. At  $a = 20 R_P$  (Fig. 11; upper left panel), satellites with  $R \approx 1$ –4 km should open a gap and undergo fast migration (eqs. [30–31]). Satellites with  $R = 3$  km migrate at rates  $\dot{a} \approx 20 \text{ km yr}^{-1}$ , close to the rate predicted in eq. (32). As the satellite radius increases from 3 km to 5–10 km, the migration rate drops considerably. These larger satellites have too much inertia to maintain the fast radial drift rate. Larger satellites with  $R \gtrsim 10$  km migrate at rates close to predicted rates for type II migration (eq. [33]).

Migration rates also depend on the semimajor axis of the satellite (Fig. 11; lower left panel). When the velocity dispersion of the disk is fixed, it is harder for smaller satellites with  $R = 3$ –4 km to open up a gap in the disk at larger  $a$  than at smaller  $a$  (eq. [30]). Thus, small satellites migrate much more slowly at large  $a$ . However,  $R_{fast}$  also increases with  $a$ . Larger satellites migrate more rapidly at larger  $a$  than at smaller  $a$ . For a larger satellite with  $R = 8$  km, the migration rate slows considerably from  $a = 60 R_P$  (roughly  $20 \text{ km yr}^{-1}$ ) to  $a = 40 R_P$  (roughly  $10 \text{ km yr}^{-1}$ ) to  $a = 20 R_P$  ( $\lesssim 1 \text{ km yr}^{-1}$ ). The relative change in the migration rate follows theoretical predictions (eqs. [32–33]).

The presence of a central binary changes these results modestly (Fig. 11; right columns). The most obvious impact of the Pluto–Charon binary is the increased velocity dispersion of disk particles. Larger velocity dispersion reduces the effectiveness of torque exchange between the satellite and disk particles in the satellite’s corotation zone, making it more difficult for a satellite to open up a gap in the disk (eq. [30]). Thus, smaller satellites migrate more slowly around a binary. There is some evidence from the simulations that larger satellites may migrate more rapidly around a binary. In these cases, larger satellites first clear their

corotation zone and halt their radial drift. As the simulation proceeds, stirring from the binary feeds some material into the corotation zone, commencing a kind of “attenuated” migration (Bromley & Kenyon 2011b). We speculate that this behavior may allow larger objects to drift more quickly through a circumbinary disk.

Simulations with a variety of disk masses confirm these general trends. Under the right conditions in disks with masses larger than  $\sim 10^{18}$  g, satellites with  $R \approx 1\text{--}20$  km can undergo fast, type II, or attenuated migration with rates ranging up to  $20 \text{ km yr}^{-1}$ . In lower mass disks, small satellites cannot clear the gap required to initiate fast migration. Although large satellites can form gaps in disks with  $M_d \lesssim 10^{18}$  g, the minimum radius required to open a gap is larger than the maximum radius for fast migration. Thus, large satellites cannot migrate in the fast mode. Instead, these objects migrate a factor of ten more slowly in the type II mode.

To test whether the disk can circularize the orbits of small satellites, we derive predicted rates for 4–10 km objects in disks with  $M_d = 1 - 10 \times 10^{17}$  g surrounding a single central object. For satellites in this size range, damping rates are independent of radius. The damping time scales with the disk mass:

$$t_{damp} \approx \frac{e}{\dot{e}} \approx 10^5 \left( \frac{10^{17} \text{ g}}{M_d} \right) \text{ yr} . \quad (48)$$

Even in a low mass disk, damping times are comparable to the formation time for 4–10 km satellites.

Estimating damping rates for satellites orbiting a central binary are complicated by precession, orbital resonances, and other dynamical issues. For the small rates indicated by simulations with a single central object, accurate estimates require a substantial investment of cpu time. When the Pluto–Charon binary has a circular orbit, dynamical friction between the satellite and disk particles will still circularize the satellite’s orbit. In a non-circular Pluto–Charon binary, the damping time probably depends on the time scale for the disk and tides to circularize the binary. Because these processes act on similar time scales, deriving the circularization time for a satellite orbit is very cpu intensive and beyond the scope of this study.

### 3.3.2. Migration of Multiple Satellites

To investigate whether ensembles of proto-satellites can migrate, we examine a second suite of simulations (Figure 12). Here, we maintain the same disk surface density distribution and focus on satellites with  $R = 4$  km or 10 km orbiting within a wide annulus spanning

orbital distances of  $35R_P$  to  $55R_P$ . Satellites and disk material orbit a compact Pluto–Charon binary with orbital separation  $a = 5 R_P$ . For material at  $35\text{--}55 R_P$ , stirring by the binary has a smaller impact than at  $20 R_P$ .

The top panel of Figure 12 follows a simulation of five 10 km satellites initially evenly spaced in orbital separation. With typical Hill radii of  $0.2 R_P$ , these satellites interact weakly among themselves. All have radii larger than  $R_{fast}$ ; migration rates are slow. Modest scattering of disk particles yields some inward or outward motion and occasional stronger gravitational interactions among the satellites. However, these satellites are fairly stable over 1000 yr and longer timescales.

Simulations with ensembles of five 4 km objects produce more complicated outcomes. With much smaller Hill radii, these satellites interact very weakly among themselves. At the onset of each simulation, however, all begin to migrate in the fast mode. Some migrate inward; others migrate outward. When neighboring satellites migrate in the same direction, migration is limited by the stirred up wake of disk particles left behind by the first satellite to pass through that portion of the disk (Bromley & Kenyon 2011b). Satellites do not cross these wakes. Thus, groups of small satellites migrating in the same direction drift radially inward/outward a small distance before the migration stalls.

Small satellites migrating in opposite directions lead to more interesting outcomes. Often, these satellites scatter one another, sometimes exchanging orbits (Fig. 12; middle panel). Depending on the sense of migration and the state of the disk after scattering, satellites may undergo multiple scattering events before settling down in roughly stable configurations within a stirred up disk. Sometimes, satellites merge. Because merged satellites are massive, they migrate more slowly and end up in a stable configuration. In our suite of simulations, mergers are less common ( $\sim 10\%$ ) than scattering events.

Simulations with a mix of 4 km and 10 km satellites also lead to interesting outcomes (Fig. 12; lower panel). If a small satellite undergoing fast migration lies between two larger satellites, its larger migration rate guarantees that it will catch up to one of its slowly moving neighbors. When it does catch up, it may ‘bounce off’ the wake of its neighbor and begin migrating in the opposite direction. In roughly half of all interactions, the larger satellite either scatters or merges with the smaller satellite. If scattering places the small satellite on an orbit with a pericenter inside  $a_{min}$ , the central binary can eject the small satellite out of the system.



### 3.3.3. Summary of Migration Calculations

For satellites with  $R \approx 4\text{--}10$  km in a disk surrounding the Pluto–Charon system, migration is ubiquitous. In a cold, geometrically thin disk, satellites in this size range can undergo fast mode or slower, type II mode migration at rates very close to those predicted by theory. These rates lead to significant radial motion,  $\sim 1\text{--}10 R_P$  in  $10^3$  yr. Scaling these rates to the hotter disks expected from the coagulation and hybrid calculations in §3.1–3.2, satellites with radii similar to P4 and P5 may migrate significantly as they grow. Although larger satellites such as Nix and Hydra migrate more slowly, radial motion of a few Pluto radii seems likely after they reach their final sizes.

Interactions between the disk and the central binary can augment or reduce migration rates. Although changes to the rates are modest, smaller (larger) satellites generally migrate more slowly (rapidly). Changes are more significant closer to the binary, where the jitter of particle orbits in the disk change the number of particles in the corotation zone of a satellite. Thus, small (large) satellites which form closer to the binary are less (more) likely to migrate than satellites which form farther away from the binary.

Ensembles of migrating satellites produce a variety of interesting dynamical phenomena. In systems with several small satellites or a mix of large and small satellites, differential migration enables large-scale scattering events and satellite mergers. When scattering places a satellite on a orbit with a pericenter smaller than  $a_{min}$ , the central binary ejects the satellite from the system. Mergers among migrating satellites allow lower mass disks to produce more massive satellites.

## 4. DISCUSSION

In §2–3, we have developed the first complete, numerical model for the formation of Pluto’s small satellites. Our approach examines two plausible origins for the icy building-blocks of these satellites, debris from the giant impact that produces the Pluto–Charon binary and material accreted from the protostellar debris disk. Canup (2011) summarizes a set of giant impact calculations which yield enough debris to produce the satellites. Our analysis indicates that a circumplanetary or circumbinary disk can capture enough mass from the protoplanetary disk to enable formation of low mass satellites. If Pluto’s satellites are more massive than their minimum allowed masses, satellite formation in debris from the giant impact is the more likely mechanism.

In each scenario, solids end up in a disk or ring surrounding the Pluto–Charon binary. For the disk/ring masses required to match the total mass in the known satellites, solids

rapidly grow into a large ensemble of proto-satellites. Dynamical interactions among the proto-satellites begin an extended period of chaotic growth where multiple satellite-satellite mergers lead to a stable system consisting of a few satellites. The number of stable satellites is inversely correlated with the starting mass: disks/rings with larger (smaller) initial masses produce fewer (more) satellites with larger (smaller) masses.

The timescale for satellite growth depends on the origin of the circumbinary debris disk. In a disk with mass  $M_d$  and surface density  $\Sigma \propto a^{-1}$ , the formation time for 1–10 km satellites is

$$t_f \approx 10^3 \left( \frac{3 \times 10^{19} \text{ g}}{M_d} \right) \left( \frac{a}{30R_P} \right)^{5/2}. \quad (49)$$

If satellites form in captured material, most of the mass lies at large distances,  $a \sim 10^3 R_P$ . Formation time are then comparable to the time scale for tidal forces to circularize and to expand the central binary,  $t_f \sim 1$  Myr. Satellites growing out of debris from the giant impact probably form much closer to the central binary, with  $t_f \approx 10^3 - 10^4$  yr.

During chaotic growth, proto-satellites radially migrate through the leftover debris. Although proto-satellites cannot fall into the Pluto–Charon binary, satellites can traverse a substantial fraction of the circumbinary disk throughout chaotic growth. Migration can induce mergers among lower mass satellites, enabling more massive satellites to form in lower mass disks. Ensembles of satellites with similar masses migrate in step with one another, enabling satellites to find stable equilibrium orbits around Pluto–Charon.

Migration rates depend on the nature of the central object. Stirring by a central binary can heat the particle disk and slow migration of satellites with radii of  $O(1)$  km. The binary may also increase migration rates of larger satellites. A possible explanation is that migration comes from the asymmetry of inward and outward satellite-disk scattering events. The binary will preferentially disturb the orbits of the inwardly scattered disk particles and prevent their return to the satellite in the same way as in the case of a single central mass. We plan additional simulations to explore this possibility.

These results suggest that the formation of low mass satellites around Pluto–Charon is a natural outcome of planet formation. Raw material for satellite production is readily available from a giant impact or the protostellar debris disk. Once the raw material collects in a disk or ring, satellite formation is ubiquitous. Stable satellites have orbital properties and a range of masses reasonably consistent with known satellites surrounding Pluto–Charon. Chaotic growth often leads to satellites with period ratios similar to those of the known satellites. Migration can also produce stable satellites in approximate resonances.

Together with previous results from Youdin et al. (2012), our calculations indicate sev-

eral conclusions about each satellite.

- The semimajor axis of P5 is almost as close as possible to the minimum stable semimajor axis  $a_{min}$ . In our framework, P5 has a low mass because (i) the debris ring had less mass close to Pluto–Charon (ii) it was scattered out of a more massive region of the ring by Nix or Hydra, or (iii) after formation at large  $a$ , it migrated into an innermost stable orbit.
- The orbit of P4 lies within a small stable region in between the orbits of Nix and Hydra (Youdin et al. 2012). More massive satellites in this region are unstable. From the coagulation and migration calculations, P4 is a smaller remnant of the accretion process.
- The masses of Nix and Hydra are consistent with the coagulation models. The central cores of either satellite could have been formed the giant impact and then accreted debris leftover from the impact.

Aside from these basic successes, our framework has one major challenge.

Once debris is in stable orbits around Pluto–Charon, the binary excites radial and epicyclic motions in orbiting particles (e.g., Lee & Peale 2006; Youdin et al. 2012). Both motions increase the radial velocity dispersion used in our calculations. For stable orbits around a circular Pluto–Charon binary, the radial oscillation is small compared to the velocity dispersion. Because collisional damping is so effective at reducing the velocity dispersion, oscillations induced by a circular binary are generally unimportant.

If the central binary has  $e \gtrsim 0.01$ , the epicyclic motion is comparable to the typical velocity dispersion during runaway and oligarchic growth. Thus, an initially eccentric Pluto–Charon binary could maintain a large velocity dispersion among debris particles, promote an extended phase of fragmentation, and frustrate the growth of proto-satellites in a circumbinary ring (see, for example, Paardekooper et al. 2012, in the context of circumbinary planets). In our calculations, however, collisional damping is very effective among small debris particles and collision fragments. Thus, damping and fragmentation can counter the impact of a central eccentric binary.

The long-term eccentricity evolution of the central binary is the main uncertainty in evaluating the relative impact of collisional damping and binary stirring. In the standard tidal picture,  $e$  damps on the tidal time scale of 0.1–10 Myr (Dobrovolskis et al. 1997). When damping is so slow, collisional grinding in a low mass disk surrounding an eccentric binary probably reduces the mass in solids considerably. Satellite formation is challenging. In both

modes of satellite formation, however, tidal damping of  $e$  is augmented by interactions with the surrounding particle disk/ring. When a ring lying close to the binary has a mass of  $\sim 10^{23}$  g – roughly the maximum inferred from giant impact calculations – the damping time scale of  $\sim 4 \times 10^3$  yr is much smaller than the tidal time scale. On this short time scale, collisional grinding reduces the disk mass to levels similar to the total masses of the small satellites. After the binary circularizes, collisional damping reduces particle velocities, enabling satellite growth.

Because rings formed during the giant impact have more mass closer to the central binary than disks generated from the protoplanetary disk, rings damp the central binary more rapidly (e.g., Lin & Papaloizou 1979, 1986a). However, satellites growing in a captured disk grow too slowly and are too far away from the central binary to care about the binary eccentricity or the damping time. Thus, both mechanisms appear viable if the Pluto–Charon binary has a large, initial eccentricity.

Constraining the impact of the central binary requires a new set of simulations (see also Paardekooper et al. 2012). Initial tests are promising and suggest that satellite formation is likely even in an eccentric binary system. Aside from these new simulations, other more comprehensive numerical simulations can help constrain satellite formation models.

- In the protostellar accretion and giant impact models, improved SPH simulations of collision outcomes would clarify the likely range of initial conditions available for satellite formation. In giant impact models, better mass resolution would yield the distribution of small particle masses within the debris. This result would enable a better evaluation of the possibility that small proto-satellites survive the giant impact more or less intact and serve as the seeds for Pluto’s small satellites.
- In accretion models, more robust SPH models (as in Canup (2011)) for the outcomes of (i) two objects colliding within the Hill sphere of a planet and (ii) a single object from the protoplanetary disk colliding with an object in the circumplanetary disk would provide better constraints on our estimates for the maximum mass of a circumplanetary disk and its evolution. These improved estimates would allow us to make a better evaluation of the viability of this model for satellite formation.
- In the aftermath of a giant impact, our estimates assume efficient collisional damping among small objects in the debris. Improving on this approach requires a detailed analytic model or a complete numerical model which shows how the properties of the circumbinary ring depend on the initial conditions of the debris and the physical interactions between debris particles.

- Once the impact debris lies in a ring surrounding the binary, many physical processes occur on roughly the same time scale. In §3, we consider three separate calculations for (i) the expansion of the ring into a disk, (ii) the growth of debris particles into satellites, and (iii) the migration of satellites through the leftover disk. Our results demonstrate that particles grow as the ring diffuses; proto-satellites migrate through the expanding disk of smaller particles as the satellites grow. Combining these three calculations into a single calculation requires merging the coagulation, diffusion, and migration codes within *Orchestra*. Our initial tests of this new algorithm are promising. We plan to describe a complete suite of simulations with this algorithm in subsequent papers.
- Aside from combining coagulation, diffusion, and migration into a single calculation, it is also necessary to include the long-term evolution of the central binary. Detailed tidal models show that the time scale for tides to circularize and expand the binary (Dobrovolskis et al. 1997) are longer than the diffusion and growth times, but similar to the time scale for chaotic growth to merge several dozen proto-satellites into the satellites we see today. These time scales are  $10 - 10^3$  times longer than the time scale for a ring of debris to damp the eccentricity and compress the orbit of Pluto–Charon. Based on our migration calculations, the interplay of tides, dynamical interactions between the debris and Pluto–Charon, and migration likely establishes the current orbits of the satellites. Thus, treating these physical processes accurately is essential for understanding the current orbital arrangement of the satellites.

Aside from informing the next generation of numerical simulations for satellite formation, the *New Horizons* mission can test several predictions of our calculations.

- In our simulations, forming four (or more) satellites orbiting Pluto–Charon requires relatively small disk masses,  $M_d \lesssim 3 \times 10^{20}$  g. Together with numerical simulations of the orbital stability of the satellites (Youdin et al. 2012), these results require satellite albedos,  $A \approx 0.4-1$ . This range for  $A$  is similar to the measured  $A \approx 0.5$  for Pluto and Charon (see Marcialis et al. 1992; Roush et al. 1996; Brown 2002; Buie et al. 2010a,b, and references therein) and much larger than the  $A$  for many Kuiper belt objects (e.g., Stansberry et al. 2008; Brucker et al. 2009). Direct measurements of  $A$  by *New Horizons* will test these constraints.
- All of the hybrid calculations leave several very small satellites orbiting beyond the orbit of Hydra. The radii of typical leftovers –  $R \lesssim 1-3$  km – imply optical magnitudes of 28 or fainter. Testing this prediction is a challenge for *Hubble Space Telescope* (Showalter et al. 2011, 2012), but satellites this size or smaller are easily visible during

the flyby of *New Horizons*. For objects with  $R \approx 1\text{--}3$  km, the most likely range of semimajor axes is  $a \approx 70\text{--}90 R_P$ . Smaller satellites might have  $a \approx 100\text{--}200 R_P$ . Both sets of small satellites should have small inclinations relative to the Pluto–Charon orbital plane, similar to the observed  $i$  for the known satellites. If smaller particles in a leftover debris disk (see next item) have sufficient mass, these outer satellites should also have circular orbits. Smaller masses in leftovers imply larger  $e$  for small outer satellites. We plan numerical calculations to test the longevity of these satellites in the tidal field of the Sun–Neptune system.

- Our calculations predict little or no mass between P5 at  $a \approx 39 R_P$  and the innermost stable orbit at  $a_{min} \approx 34 R_P$  (see also Youdin et al. 2012). If this region contains debris from the giant impact or from occasional impacts of small Kuiper belt objects with the satellites, *New Horizons* might detect a low density stream of material from  $a_{min}$  to Charon’s orbit at  $a_C \approx 17 R_P$ . As with circumbinary gaseous disks, the properties of this stream might yield constraints on the internal viscosity of small solid objects orbiting Pluto–Charon (Artymowicz & Lubow 1996).
- All of the diffusion calculations predict ensembles of smaller particles,  $R \lesssim 0.01\text{--}10$  m, in an extended disk well beyond the orbits of the known satellites. For a mass of  $\sim 10^{15}$  g in leftover small particles with typical radius  $R$ , the predicted optical depth of the disk is  $\tau_l \sim 10^{-10} R^{-1}$  at semimajor axes  $a \approx 70\text{--}200 R_P$ . Larger (smaller) disk masses imply proportionately larger (smaller) optical depths. Although this mass is significant, the predicted optical depth is much smaller than the  $\tau \lesssim 10^{-7}$  estimated for clouds of  $1\text{--}100 \mu\text{m}$  particles produced by impacts of Kuiper belt objects on the known satellites (Poppe & Horányi 2011). *New Horizons* measurements of the optical depths of small particles surrounding the known satellites and at larger distances should place interesting constraints on the long-term evolution of the satellite system and its interactions with the Kuiper belt.
- Measuring the outer radius of the extended disk tests the capture hypothesis. In this picture, most of the mass lies at large semimajor axes,  $a \approx 1000 R_P$ . Identifying any material at  $a \approx 100\text{--}1000 R_P$  suggests that capture is a viable mechanism. The amount of material at these distances provides a measure of the capture efficiency (see eq. [8]).
- Composition data from *New Horizons* should also enable tests of the formation scenarios. In the giant impact picture, satellites form out of the same material as Charon. Depending on relative contamination from impacting Kuiper belt objects (e.g. Stern et al. 2006; Poppe & Horányi 2011), satellites should have roughly the same composition as Charon. In the circumplanetary accretion scenario, satellites form out of the collisional debris of Kuiper belt objects captured by Pluto, Pluto–Charon, or both. The broad

variety of physical characteristics of Kuiper belt objects (see Barucci et al. 2008) suggests that satellites grown from the debris of Kuiper belt objects should have very different compositions from satellites grown from the debris of a giant impact (see also Stern 2009). Thus, direct measurement of the compositions of individual satellites and gradients in the composition among any smaller satellites and debris should constrain both scenarios for satellite formation.

- Observed shapes of satellites might test formation models. In general, large fragments from the impact should be more irregular than satellites grown from a circumbinary disk/ring of much smaller particles.

To develop predicted configurations for the Pluto–Charon system during a *New Horizons* encounter, we ran  $n$ -body simulations of Pluto–Charon, the known small satellites, and several predicted satellites embedded within a disk of two million massless tracer particles. After 20 yr (roughly 1000 orbits of the inner binary), the satellites have cleared many tracers from their orbits (Fig. 13). On longer time scales, the satellites clear their orbits completely (see also Youdin et al. 2012). The predicted optical depth and extent of the disk depends on (i) the number of small satellites beyond Hydra, (ii) the viscosity of disk particles, and (iii) the amount of mass in small particles produced from recent impacts on the satellites (e.g., Stern 2009; Poppe & Horányi 2011). If (i) there are few small satellites, (ii) disk particles have low viscosity, and (iii) impacts are common, we expect *New Horizons* to detect a modest disk of small particles with rings and gaps similar to those shown in the Fig. If, however, (i) there are many small satellites beyond Hydra’s orbit, (ii) disk particles have large viscosity, and (iii) impacts are relatively rare, the *New Horizons* encounter may reveal little disk material. Once *New Horizons* has mapped the Pluto–Charon system completely, improved numerical simulations will enable a more complete examination of the formation and history of the satellite system.

## 5. SUMMARY

We describe a theoretical framework for the origin of Pluto’s small satellites in the context of two scenarios, (i) a giant impact that produces the Pluto–Charon binary (e.g., Canup 2011) or (ii) accretion from material in the protoplanetary disk (e.g., Lithwick & Wu 2008). Our main results follow.

- Throughout the early history of the solar system, giant impacts capable of producing the Pluto–Charon binary have a frequency of 1 per 100–300 Myr. These impacts

leave behind enough debris to enable satellite formation (Canup 2011). After impact, Charon captures  $\sim 50\%$  of the debris. Collisional damping enables debris particles ejected by Charon to attain bound orbits at a few times the orbital separation of the Pluto–Charon binary.

- Capturing debris from collisions of Kuiper belt objects within the Hill sphere of Pluto (prior to impact) or Pluto–Charon (after impact) can produce a circumplanetary disk with a maximum mass of roughly  $3 \times 10^{19}$  g. Unless the growth of satellites in the captured material is nearly 100% efficient and the current satellites have albedo  $A \approx 1$ , satellites are more likely to form in debris from the impact than in material captured from the protoplanetary disk.
- In a ring of small particles,  $R \lesssim 0.1$  km, surrounding Pluto–Charon, satellites with  $R \approx 10\text{--}80$  km form rapidly on a time scale of  $10^3\text{--}10^4$  yr. The formation time is similar to the migration time scale and the viscous time scale. Thus, satellites grow and migrate in a viscously spreading disk surrounding Pluto–Charon.
- After the impact, objects with  $R \approx 1\text{--}10$  km might survive collisional disruption during the ejection process. Calculations of disks with small particles and a few seeds produce fewer satellites with larger masses than calculations with small particles alone.
- Radial migration encourages mergers of small satellites within an evolving disk surrounding Pluto–Charon.
- Scattering events among differentially migrating satellites sometimes places objects on orbits with pericenters close to the central binary. Unless interactions with disk particles can damp the orbit, the Pluto–Charon binary ejects these satellites from the system.
- For identical masses of the central planet(s), the surrounding disk, and a small satellite embedded in the disk, migration rates around a binary planet differ slightly from those around a single planet. For Pluto–Charon, the drift rate of a satellite the size of P5 maybe be as high as  $0.5\text{ km yr}^{-1}$ .
- For a disk with mass sufficient to produce the satellites, the time scale for dynamical interactions to damp  $e$  and reduce  $a$  for the central binary is shorter than the tidal time scale. Thus, an accurate model for the tidal evolution of Pluto–Charon must include the evolution of the circumplanetary ring that includes growing and migrating satellites.



- The current number of small Pluto–Charon satellites strongly favors low mass disks (see also Youdin et al. 2012). In our calculations, disks with masses  $M_d \approx 3 - 10 \times 10^{19}$  have the best chance at producing 3–5 satellites with orbital semimajor axes  $a \approx 40$ – $60 R_P$ . Matching observations requires Pluto’s satellites to have albedos  $A \approx 0.4$ – $1$ . *New Horizons* data will test this prediction.
- Model satellites produced in formation calculations have orbital  $i$  close to those observed, but the typical  $e$  is generally too large. Orbital migration can reduce  $e$  to acceptable levels.
- The calculations predict a few very small,  $R \lesssim 1$ – $3$  km, satellites and an extended disk of even smaller particles,  $R \approx 1$ – $100$  cm, beyond the current orbit of Hydra. Detecting these satellites and the disk from the ground is very challenging. If they are present, *New Horizons* should detect them easily.
- Material lying between P5 and the innermost stable orbit around Pluto–Charon might produce a stream of small particles from the circumbinary disk to Charon’s orbit.

Our results demonstrate that numerical calculations can produce simulated satellite systems with properties reasonably close to those observed. Prior to the *New Horizons* flyby of Pluto–Charon, we expect to refine the predictions considerably. Once *New Horizons* probes the masses, orbital architecture, and composition of the Pluto–Charon binary, a rich interplay between the data and the numerical simulations will enable a much more robust theory for the formation of satellites (planets) in binary planetary (stellar) systems.

We acknowledge generous allotments of computer time on the NASA ‘discover’ cluster and the SI ‘hydra’ cluster. Advice and comments from M. Geller and A. Youdin greatly improved our presentation. Portions of this project were supported by the *NASA Astrophysics Theory* and *Origins of Solar Systems* programs through grant NNX10AF35G and the *NASA Outer Planets Program* through grant NNX11AM37G.

## REFERENCES

- Adachi, I., Hayashi, C., & Nakazawa, K. 1976, *Progress of Theoretical Physics*, 56, 1756
- Araki, S., & Tremaine, S. 1986, *Icarus*, 65, 83
- Artymowicz, P., & Lubow, S. H. 1996, *ApJ*, 467, L77

- Asphaug, E., Agnor, C. B., & Williams, Q. 2006, *Nature*, 439, 155
- Barge, P., & Pellat, R. 1990, *Icarus*, 85, 481
- Barucci, M. A., Boehnhardt, H., Cruikshank, D. P., & Morbidelli, A. 2008, *The Solar System Beyond Neptune*, ed. Barucci, M. A., Boehnhardt, H., Cruikshank, D. P., & Morbidelli, A. (University of Arizona Press, Tucson, AZ)
- Bath, G. T., & Pringle, J. E. 1981, *MNRAS*, 194, 967
- Benz, W., & Asphaug, E. 1999, *Icarus*, 142, 5
- Bromley, B. C., & Kenyon, S. J. 2006, *AJ*, 131, 2737
- . 2011a, *ApJ*, 731, 101
- . 2011b, *ApJ*, 735, 29
- . 2013, *ApJ*
- Brown, M. E. 2002, *Annual Review of Earth and Planetary Sciences*, 30, 307
- Brucker, M. J., Grundy, W. M., Stansberry, J. A., Spencer, J. R., Sheppard, S. S., Chiang, E. I., & Buie, M. W. 2009, *Icarus*, 201, 284
- Buie, M. W., Grundy, W. M., Young, E. F., Young, L. A., & Stern, S. A. 2006, *AJ*, 132, 290
- . 2010a, *AJ*, 139, 1117
- . 2010b, *AJ*, 139, 1128
- Burns, J. A., Lamy, P. L., & Soter, S. 1979, *Icarus*, 40, 1
- Canup, R. M. 2005, *Science*, 307, 546
- . 2011, *AJ*, 141, 35
- Canup, R. M., & Ward, W. R. 2002, *AJ*, 124, 3404
- Chambers, J. E. 2001, *Icarus*, 152, 205
- Chambers, J. E., & Wetherill, G. W. 1998, *Icarus*, 136, 304
- Charnoz, S., Salmon, J., & Crida, A. 2010, *Nature*, 465, 752
- Charnoz, S., et al. 2011, *Icarus*, 216, 535

- Christy, J. W., & Harrington, R. S. 1978, *AJ*, 83, 1005
- Cionco, R. G., & Brunini, A. 2002, *MNRAS*, 334, 77
- Daisaka, H., Tanaka, H., & Ida, S. 2001, *Icarus*, 154, 296
- Dobrovolskis, A. R., Peale, S. J., & Harris, A. W. 1997, *Dynamics of the Pluto-Charon Binary*, ed. S. A. Stern & D. J. Tholen, 159
- Dohnanyi, J. S. 1969, *J. Geophys. Res.*, 74, 2531
- Dominik, C., & Decin, G. 2003, *ApJ*, 598, 626
- Durda, D. D., & Stern, S. A. 2000, *Icarus*, 145, 220
- Durisen, R. H., Cramer, N. L., Murphy, B. W., Cuzzi, J. N., Mullikin, T. L., & Cederbloom, S. E. 1989, *Icarus*, 80, 136
- Farinella, P., Milani, A., Nobili, A. M., & Valsecchi, G. B. 1979, *Moon and Planets*, 20, 415
- Goldreich, P., Lithwick, Y., & Sari, R. 2002, *Nature*, 420, 643
- . 2004, *ARA&A*, 42, 549
- Goldreich, P., & Lynden-Bell, D. 1965, *MNRAS*, 130, 97
- Goldreich, P., & Tremaine, S. 1982, *ARA&A*, 20, 249
- Greenberg, R., Weidenschilling, S. J., Chapman, C. R., & Davis, D. R. 1984, *Icarus*, 59, 87
- Hahn, J. M., & Malhotra, R. 1999, *AJ*, 117, 3041
- Hayashi, C. 1981, *Progress of Theoretical Physics Supplement*, 70, 35
- Heppenheimer, T. A. 1974, *Icarus*, 22, 436
- Holman, M. J., & Wiegert, P. A. 1999, *AJ*, 117, 621
- Hornung, P., Pellat, R., & Barge, P. 1985, *Icarus*, 64, 295
- Housen, K. R., & Holsapple, K. A. 2011, *Icarus*, 211, 856
- Ida, S., Bryden, G., Lin, D. N. C., & Tanaka, H. 2000, *ApJ*, 534, 428
- Ida, S., Kokubo, E., & Makino, J. 1993, *MNRAS*, 263, 875
- Ida, S., & Makino, J. 1993, *Icarus*, 106, 210

- Kennedy, G. M., & Wyatt, M. C. 2011, *MNRAS*, 412, 2137
- Kenyon, S. J. 2002, *PASP*, 114, 265
- Kenyon, S. J., & Bromley, B. C. 2001, *AJ*, 121, 538
- . 2002, *AJ*, 123, 1757
- . 2004a, *AJ*, 127, 513
- . 2004b, *ApJ*, 602, L133
- . 2004c, *AJ*, 128, 1916
- . 2005, *AJ*, 130, 269
- . 2006, *AJ*, 131, 1837
- . 2008, *ApJS*, 179, 451
- . 2010, *ApJS*, 188, 242
- . 2012, *AJ*, 143, 63
- Kenyon, S. J., Bromley, B. C., O’Brien, D. P., & Davis, D. R. 2008, in *The Solar System Beyond Neptune*, ed. Barucci, M. A., Boehnhardt, H., Cruikshank, D. P., & Morbidelli, A. (University of Arizona Press, Tucson, AZ), 293–313
- Kenyon, S. J., & Luu, J. X. 1998, *AJ*, 115, 2136
- . 1999, *AJ*, 118, 1101
- Kirsh, D. R., Duncan, M., Brasser, R., & Levison, H. F. 2009, *Icarus*, 199, 197
- Kobayashi, H., & Tanaka, H. 2010, *Icarus*, 206, 735
- Kokubo, E., & Ida, S. 1995, *Icarus*, 114, 247
- . 1996, *Icarus*, 123, 180
- Kominami, J., & Ida, S. 2002, *Icarus*, 157, 43
- Kominami, J. D., Makino, J., & Daisaka, H. 2011, *PASJ*, 63, 1331
- Lee, M. H., & Peale, S. J. 2006, *Icarus*, 184, 573
- Leinhardt, Z. M., Marcus, R. A., & Stewart, S. T. 2010, *ApJ*, 714, 1789

- Leinhardt, Z. M., & Stewart, S. T. 2009, *Icarus*, 199, 542
- Leinhardt, Z. M., Stewart, S. T., & Schultz, P. H. 2008, in *The Solar System Beyond Neptune*, ed. Barucci, M. A., Boehnhardt, H., Cruikshank, D. P., & Morbidelli, A. (University of Arizona Press, Tucson, AZ), 195–211
- Lin, D. N. C., & Papaloizou, J. 1979, *MNRAS*, 188, 191
- . 1986a, *ApJ*, 307, 395
- . 1986b, *ApJ*, 309, 846
- Lithwick, Y., & Wu, Y. 2008, ArXiv e-prints
- Love, A. E. H. 1944, *Treatise on the Mathematical Theory of Elasticity*, 4th edition (Cambridge University Press, Cambridge, U. K.)
- Lynden-Bell, D., & Pringle, J. E. 1974, *MNRAS*, 168, 603
- Malhotra, R. 1993, *Nature*, 365, 819
- Marcialis, R. L., Lebofsky, L. A., Disanti, M. A., Fink, U., Tedesco, E. F., & Africano, J. 1992, *AJ*, 103, 1389
- Martin, R. G., & Lubow, S. H. 2011, *MNRAS*, 413, 1447
- McKinnon, W. B. 1989, *ApJ*, 344, L41
- Murray, C. D., & Dermott, S. F. 1999, *Solar system dynamics* (Princeton: Princeton University Press)
- Nagasawa, M., Lin, D. N. C., & Thommes, E. 2005, *ApJ*, 635, 578
- Nelson, R. P., & Papaloizou, J. C. B. 2004, *MNRAS*, 350, 849
- Noll, K. S., Grundy, W. M., Chiang, E. I., Margot, J.-L., & Kern, S. D. 2008, in *The Solar System Beyond Neptune*, ed. Barucci, M. A., Boehnhardt, H., Cruikshank, D. P., & Morbidelli, A. (The University of Arizona Press: University of Arizona Press, Tucson, AZ), 345–363
- O’Brien, D. P., & Greenberg, R. 2003, *Icarus*, 164, 334
- Ogihara, M., & Ida, S. 2012, *ApJ*, 753, 60
- Ohtsuki, K. 1992, *Icarus*, 98, 20

- Ohtsuki, K., Stewart, G. R., & Ida, S. 2002, *Icarus*, 155, 436
- Paardekooper, S.-J., Leinhardt, Z. M., Thébault, P., & Baruteau, C. 2012, *ApJ*, 754, L16
- Peale, S. J. 1999, *ARA&A*, 37, 533
- Peale, S. J., Cheng, W. H., & Lee, M. H. 2011, in *EPSC-DPS Joint Meeting 2011*, 665
- Pires dos Santos, P. M., Morbidelli, A., & Nesvorný, D. 2012, *Celestial Mechanics and Dynamical Astronomy*, 114, 341
- Poppe, A., & Horányi, M. 2011, *Planet. Space Sci.*, 59, 1647
- Press, W. H., Teukolsky, S. A., Vetterling, W. T., & Flannery, B. P. 1992, *Numerical recipes in FORTRAN. The art of scientific computing* (Cambridge: University Press)
- Pringle, J. E. 1981, *ARA&A*, 19, 137
- . 1991, *MNRAS*, 248, 754
- Rafikov, R. R. 2001, *AJ*, 122, 2713
- Roush, T. L., Cruikshank, D. P., Pollack, J. B., Young, E. F., & Bartholomew, M. J. 1996, *Icarus*, 119, 214
- Salmon, J., Charnoz, S., Crida, A., & Brahic, A. 2010, *Icarus*, 209, 771
- Sasaki, T., Stewart, G. R., & Ida, S. 2010, *ApJ*, 714, 1052
- Showalter, M. R., Hamilton, D. P., Stern, S. A., Weaver, H. A., Steffl, A. J., & Young, L. A. 2011, *IAU Circ.*, 9221, 1
- Showalter, M. R., et al. 2012, *IAU Circ.*, 9253, 1
- Shu, F. H., & Stewart, G. R. 1985, *Icarus*, 62, 360
- Sicardy, B., et al. 2006, *Nature*, 439, 52
- Stansberry, J., Grundy, W., Brown, M., Cruikshank, D., Spencer, J., Trilling, D., & Margot, J.-L. 2008, in *The Solar System Beyond Neptune*, ed. Barucci, M. A., Boehnhardt, H., Cruikshank, D. P., & Morbidelli, A. (University of Arizona Press, Tucson, AZ), 161–179
- Stern, S. A. 2008, *Space Sci. Rev.*, 140, 3

- . 2009, *Icarus*, 199, 571
- Stern, S. A., & Colwell, J. E. 1997, *AJ*, 114, 841
- Stern, S. A., et al. 2006, *Nature*, 439, 946
- Süli, Á., & Zsigmond, Z. 2009, *MNRAS*, 398, 2199
- Tanaka, H., & Ida, S. 1996, *Icarus*, 120, 371
- Tholen, D. J., Buie, M. W., Grundy, W. M., & Elliott, G. T. 2008, *AJ*, 135, 777
- Toomre, A. 1964, *ApJ*, 139, 1217
- Tsukamoto, Y., & Makino, J. 2007, *ApJ*, 669, 1316
- Ward, W. R. 1997, *Icarus*, 126, 261
- Ward, W. R., & Canup, R. M. 2006, *Science*, 313, 1107
- . 2010, *AJ*, 140, 1168
- Weaver, H. A., et al. 2006, *Nature*, 439, 943
- Weidenschilling, S. J. 1977a, *MNRAS*, 180, 57
- . 1977b, *Ap&SS*, 51, 153
- . 1989, *Icarus*, 80, 179
- . 2002, *Icarus*, 160, 212
- Weidenschilling, S. J., Spaute, D., Davis, D. R., Marzari, F., & Ohtsuki, K. 1997, *Icarus*, 128, 429
- Wetherill, G. W., & Stewart, G. R. 1989, *Icarus*, 77, 330
- . 1993, *Icarus*, 106, 190
- Williams, D. R., & Wetherill, G. W. 1994, *Icarus*, 107, 117
- Winter, S. M. G., Winter, O. C., Guimarães, A. H. F., & Silva, M. R. 2010, *MNRAS*, 404, 442
- Wyatt, M. C. 2008, *ARA&A*, 46, 339

Wyatt, M. C., Dermott, S. F., Telesco, C. M., Fisher, R. S., Grogan, K., Holmes, E. K., & Piña, R. K. 1999, *ApJ*, 527, 918

Youdin, A. N., & Kenyon, S. J. 2012, ArXiv e-prints

Youdin, A. N., Kratter, K. M., & Kenyon, S. J. 2012, ArXiv e-prints

Young, E. F., & Binzel, R. P. 1994, *Icarus*, 108, 219

Young, E. F., Young, L. A., & Buie, M. 2007, in *Bulletin of the American Astronomical Society*, Vol. 39, AAS/Division for Planetary Sciences Meeting Abstracts #39, 541



Table 1. Key for Frequently Used Symbols

Symbol	Definition
$R, M, \rho, A, v_{esc}$	radius, mass, mass density, albedo, and escape velocity of a solid particle
$a, e, i, \Omega, T$	semimajor axis, eccentricity, inclination, angular velocity, and period of an orbit
$v$	orbital velocity
$R_H$	Hill radius
$R_P, M_P, M_C, q_{PC}$	radius, mass of Pluto; mass of Charon; mass ratio of Pluto–Charon
$a_{PC}, e_{PC}, \Omega_{PC}, T_{PC}$	orbital parameters of Pluto–Charon binary
$\omega, t_r$	angular rotational velocity and rotational period of Pluto or Charon
$t_{exp}, t_{sync}$	time for Pluto–Charon orbit to expand or to synchronize with rotational period
$\Sigma, x_m$	surface density and mass scaling factor, $\Sigma \propto x_m a^{-n}$
$\nu, t_\nu$	viscosity, viscous time scale; $t_\nu \approx a^2/\nu$
$a_{min}$	minimum stable orbital distance from the Pluto–Charon binary
$H_z, v_z, v_r$	vertical scale height and velocity dispersion; radial velocity dispersion
$\tau_d, \tau_p$	optical depth of circumplanetary ('d') or protoplanetary ('p') disk; $\tau \propto \Sigma/R$
$a_d, M_d, \delta$	radial distance, mass, and fractional width of debris ring
$t_{df}$	time for dynamical friction to damp orbital eccentricity of disk particles
$R_{min}, R_{max}$	size of smallest, largest particle
$t_c, \sigma, f_g$	collision time, collisional cross-section, gravitational focusing factor
$b, v_{imp}$	impact parameter and impact velocity
$p, f$	probability for giant impact, efficiency factor for accretion
$Q_c, Q_D^*$	collision energy; energy required to disperse half the mass to infinity
$m_{pro}$	promotion mass in hybrid code; the $n$ -body code tracks objects with $m > m_{pro}$
$t_{pro}, t_f$	time scale for satellites to reach the promotion mass or their final mass
$N_s, N_P$	number of satellites or Pluto-mass objects formed in simulations
$R_{gap}$	Hill radius of satellite able to open a gap in the disk
$R_{fast}$	maximum Hill radius of satellite able to migrate in the fast mode
$\dot{a}_{fast}, \dot{a}_{II}$	migration rate in the fast or type II mode

Table 2. Physical Processes Involved in Satellite Formation

Phase	Physical Process	Section
<i>Model overview</i>		
Giant Impact	Pluto-Charon mass objects grow in protoplanetary disk	2.1
	Pluto-Charon mass objects collide in disk	2.1
	Circumplanetary disk evolution	2.2
Debris Ejection	Pluto-Charon accrete some debris	2.3
	Pluto-Charon eject some debris	2.3
Ring Formation	Collisions circularize orbits of debris particles	2.3
	Tidal forces circularize and expand the binary orbit	2.4
	Debris circularizes binary orbit	2.4
	Viscosity spreads ring into disk	2.5.1
Satellite Growth	Collisions destroy largest debris particles	2.5.2
	Collisional damping reduces velocity dispersions	2.5.3
	Satellites begin to grow	2.5.3
Migration	Fast migration of small satellites	2.6
	Slow migration of large satellites	2.6
<i>Numerical Simulations</i>		
Viscous Disk	Evolution of material captured from protoplanetary disk	3.1.2
	Evolution of debris from the giant impact	3.1.3
Satellite Growth	Pure coagulation calculations of small satellites	3.2.1
	Hybrid calculations of large satellites	3.2.2
Migration	Migration of single satellites	3.3.1
	Migration of multiple satellites	3.3.2
	Mergers	3.3.2

Table 3. Fragmentation parameters for coagulation calculations

Type	$Q_b$	$\beta_b$	$Q_g$	$\beta_g$
Weak	$2 \times 10^5$	-0.4	0.22	1.30
Strong	$10^1-10^5$	+0.0	1.5	1.25
Very Strong	$10^1-10^5$	+0.0	$10^{-4}$	2.00

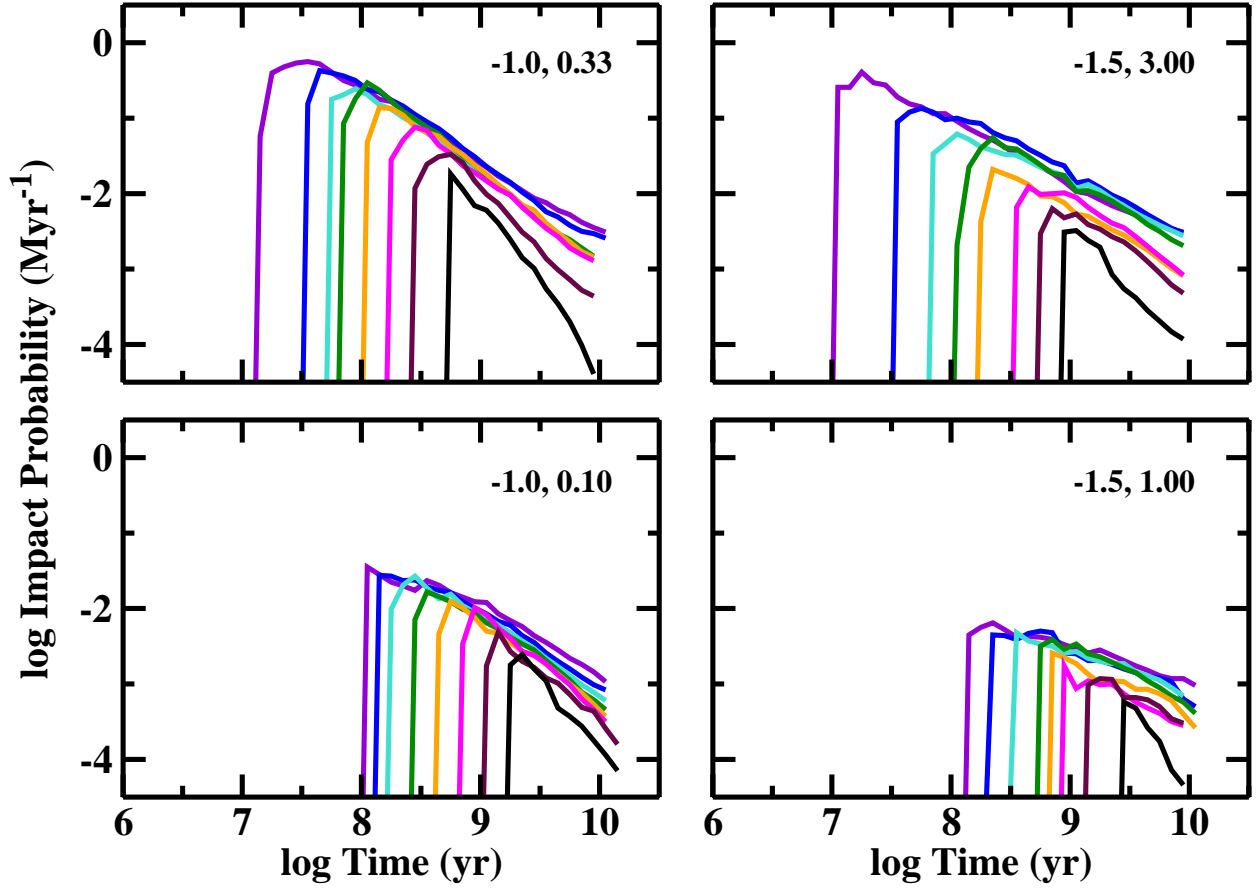


Fig. 1.— Probability of giant impacts in protoplanetary disks. Giant impacts require collisions between a massive target,  $m_t \gtrsim 10^{25}$  g, and a projectile with  $m_p \gtrsim 0.3m_t$ . In each panel, the legend lists the slope of the radial surface density profile  $n$  and the relative disk mass  $x_m$ . Colored curves illustrate the time evolution of the impact probability per Myr for disk annuli at  $a = 30-36$  AU (violet),  $a = 36-44$  AU (blue),  $a = 44-54$  AU (turquoise),  $a = 54-66$  AU (green),  $a = 66-80$  AU (orange),  $a = 80-100$  AU (magenta),  $a = 100-120$  AU (maroon), and  $a = 120-150$  AU (black). Giant impacts happen earlier and more frequently in more massive disks.

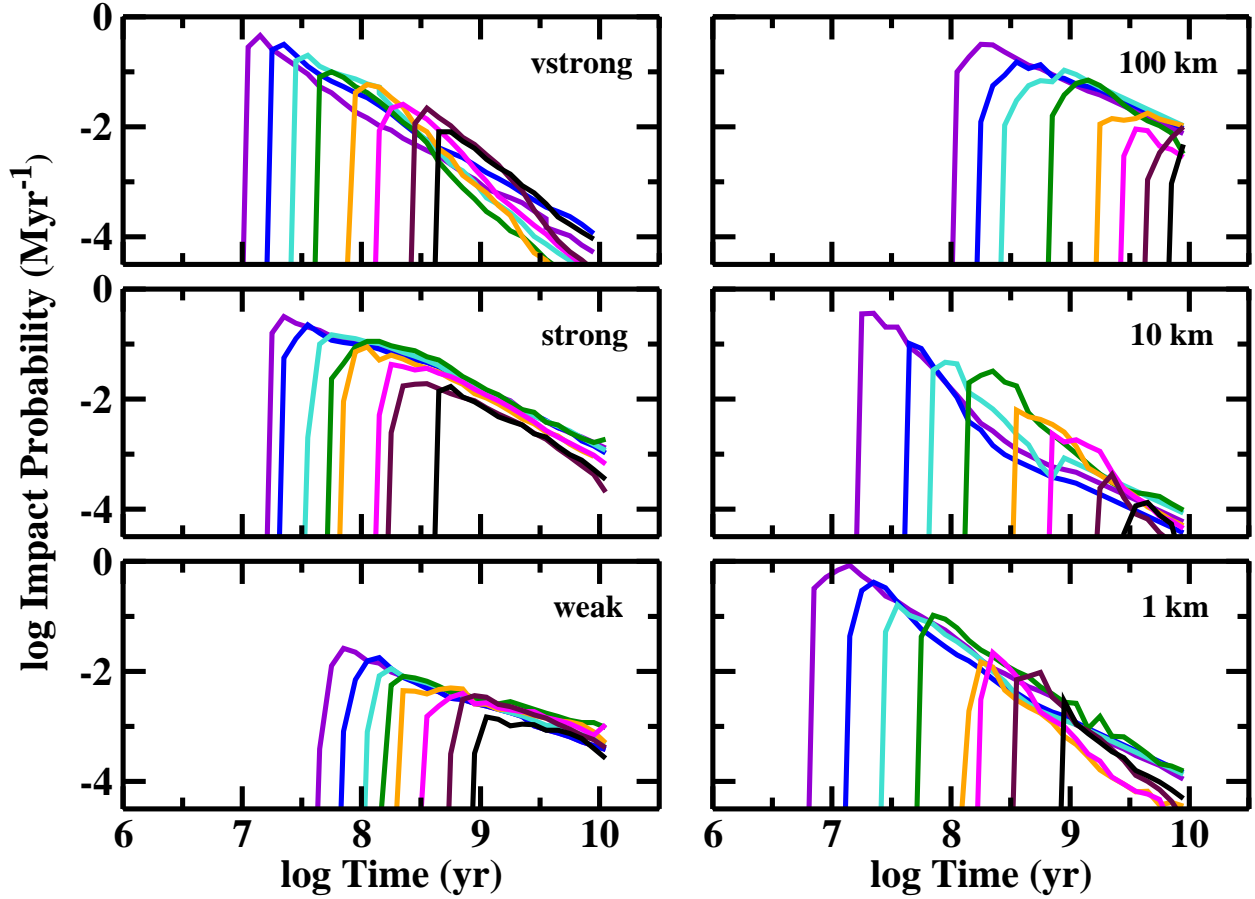


Fig. 2.— As in Fig. 1 for disks with  $n = 1.5$  and  $x_m = 1.00$ . Left panels: results for calculations with  $R_0 = 1$  km and different fragmentation parameters. Right panels: results for calculations with weak planetesimals and  $R_0 = 1, 10,$  and  $100$  km. Because larger objects form more frequently when planetesimals are strong, giant impacts are more common in calculations with strong planetesimals. Planets form faster when planetesimals are initially smaller; thus, giant impacts occur earlier when  $R_0$  is smaller.

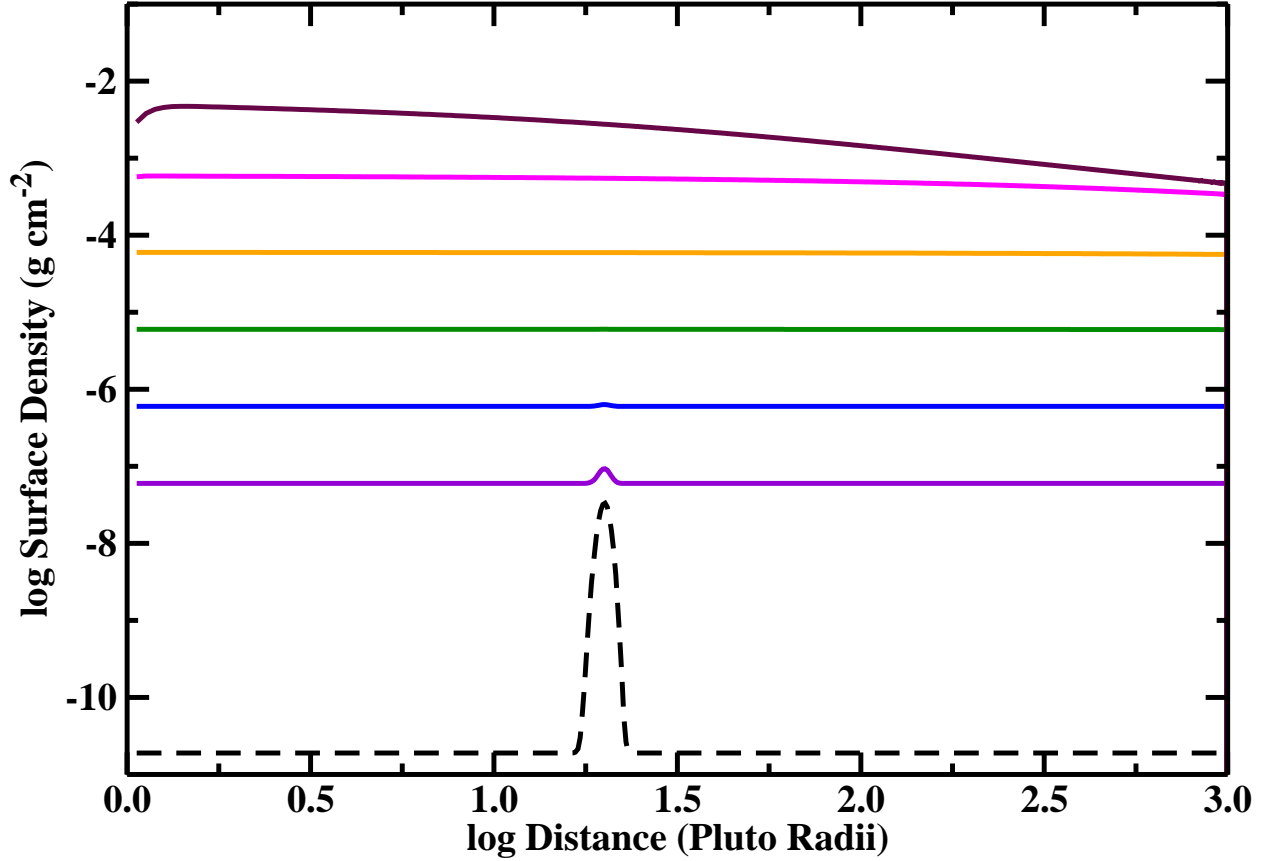


Fig. 3.— Surface density profiles in a circumplanetary disk surrounding a Pluto-mass protoplanet. The disk has a gaussian initial surface density with a mass of  $10^{11}$  g centered at  $20 R_P$ . Collisions from material in the protoplanetary disk augment and deplete the surface density according to the prescription in eq. (39). Mass addition gradually erases the initial conditions, yielding a roughly constant surface density at all radii at  $10^4$  yr (violet curve),  $10^5$  yr (blue curve),  $10^6$  yr (green curve),  $10^7$  yr (orange curve), and  $10^8$  yr (magenta curve). As the disk mass reaches a steady-state at  $10^9$  yr (maroon curve), the surface density peaks close to the central protoplanet.

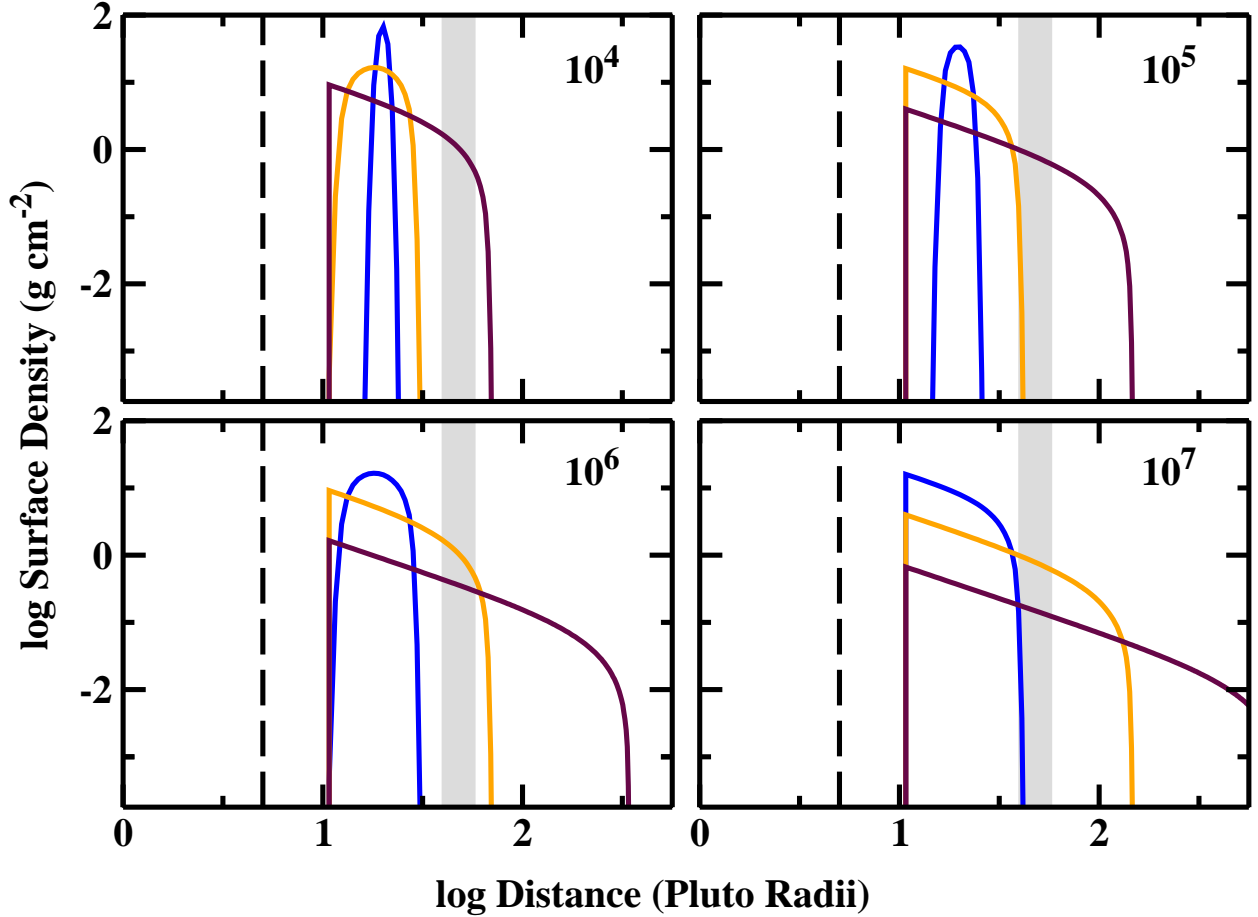


Fig. 4.— Surface density evolution in a circumplanetary disk with  $M_d = 3 \times 10^{20}$  g surrounding the Pluto–Charon binary at  $10^4$  yr (upper left panel),  $10^5$  yr (upper right panel),  $10^6$  yr (lower left panel), and  $10^7$  yr (lower right panel). The calculations assume a constant  $a_{PC} = 5 R_P$  (vertical dashed line in each panel). The vertical grey bar indicates separations occupied by the satellites P5, Nix, P4, and Hydra. Solid colored lines indicate the surface density distribution for 0.1 km particles with radial velocity dispersion  $v_r = 5$  cm s $^{-1}$  (blue), 50 cm s $^{-1}$  (orange), and 500 cm s $^{-1}$  (maroon). The binary truncates the disk at a distance of  $2 a_{PC}$  ( $10 R_P$ ) from Pluto. Disks with large  $v_r$  expand more rapidly than disks with small  $v_r$ . The outer radii of the disks reach the orbits of the small satellites in  $10^5$ – $10^7$  yr.

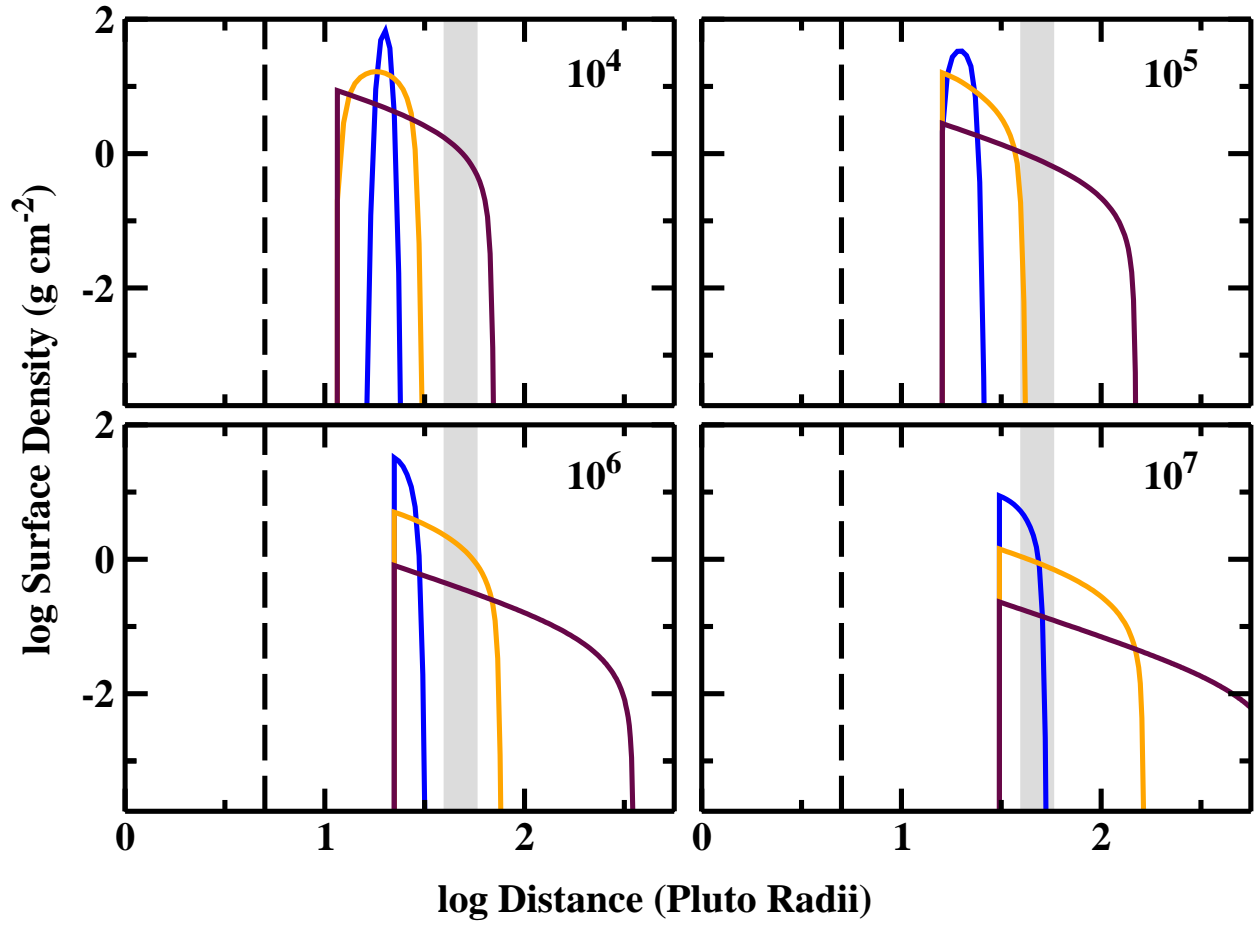


Fig. 5.— As in Fig. 4 for an expanding Pluto–Charon binary. In each panel, the dashed vertical line indicates the semimajor axis of Charon’s orbit. Compared to calculations without an expanding binary, the disks in these calculations are more compressed but reach the orbits of the small satellites at similar times.



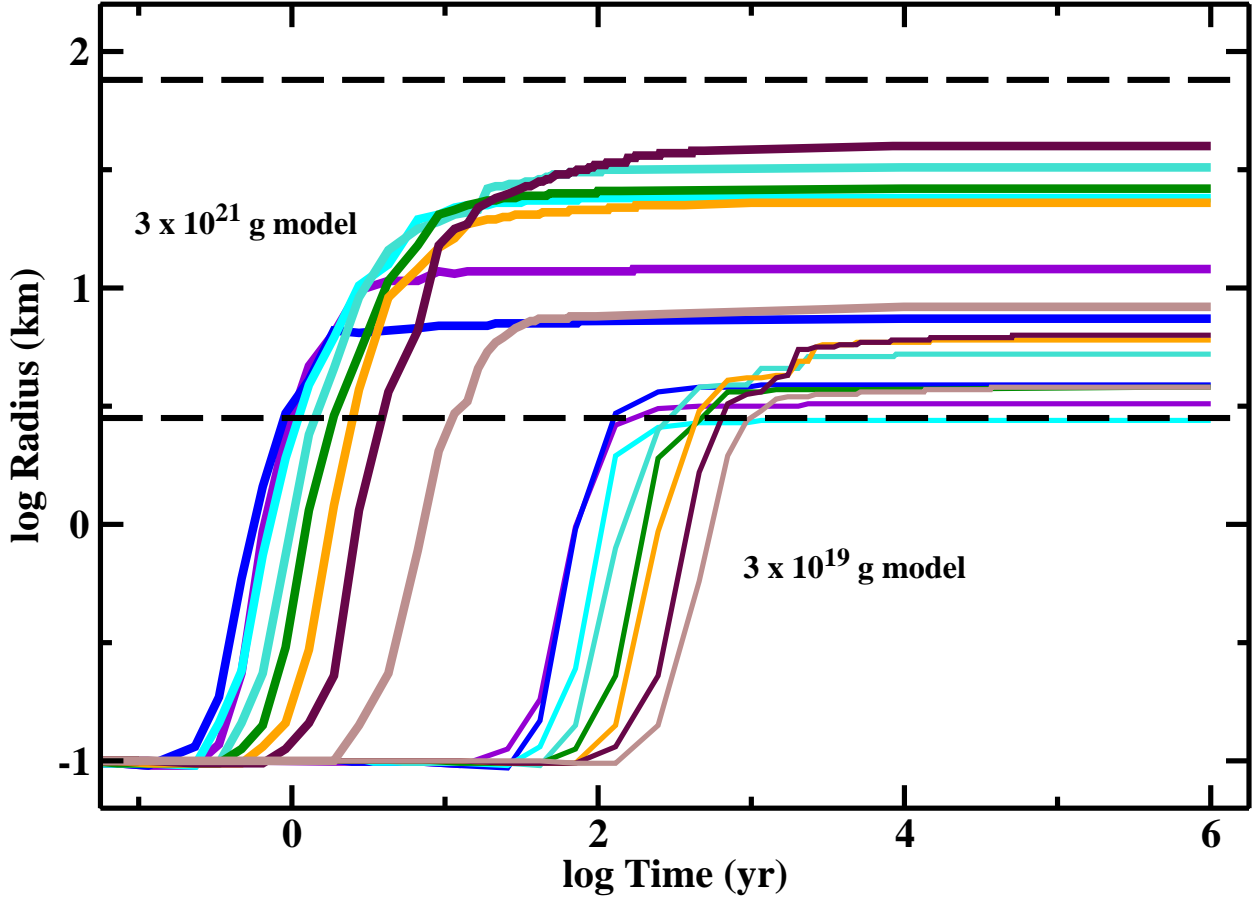


Fig. 6.— Radius evolution for satellites in a disk surrounding the Pluto–Charon binary. The dashed lines indicate the lower limit for the radius of P5 ( $A = 1$ ) and the upper limit for the radius of Hydra ( $A = 0.04$ ) assuming a mass density  $\rho = 1 \text{ g cm}^{-3}$ . The thin (thick) lines plot results for a model with an initial disk mass of  $M_d = 3 \times 10^{19} \text{ g}$  ( $M_d = 3 \times 10^{21} \text{ g}$ ) in solid objects with initial radii of 0.1 km and smaller. Each line indicates the radius evolution for the largest object in annuli at  $17.5 R_P$  (violet),  $20 R_P$  (blue),  $23 R_P$  (cyan),  $26.5 R_P$  (turquoise),  $30.5 R_P$  (green),  $35 R_P$  (orange),  $40.5 R_P$  (maroon), and  $46.5 R_P$  (brown). Satellites grow faster in more massive disks. The range of model radii span the range inferred for satellites of Pluto–Charon.

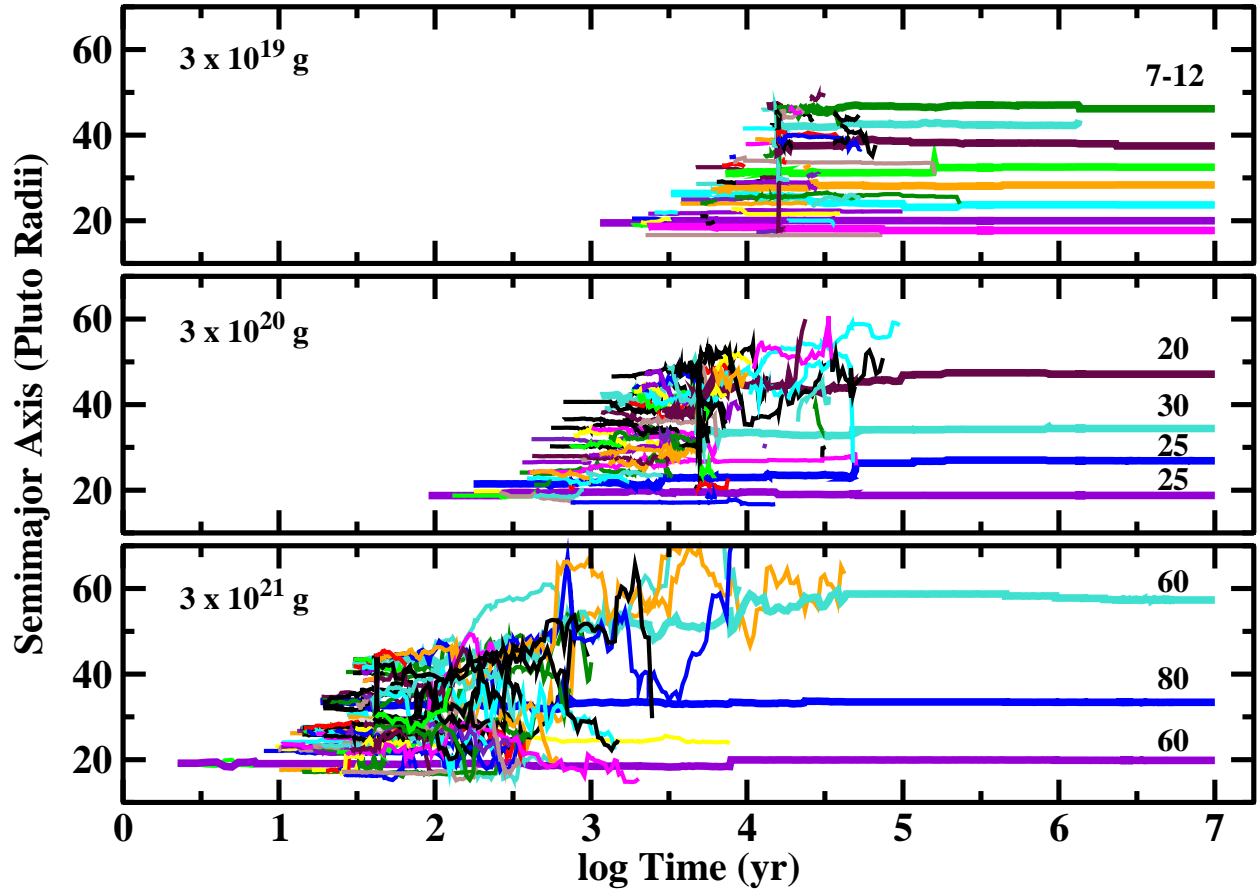


Fig. 7.— Semimajor axis evolution for satellites in a disk surrounding Pluto–Charon. The upper left corner of each panel lists the initial disk mass. Along the right edge of each panel, numbers indicate the radii (in km) of each satellite. More massive disks produce fewer, larger satellites than less massive disks.

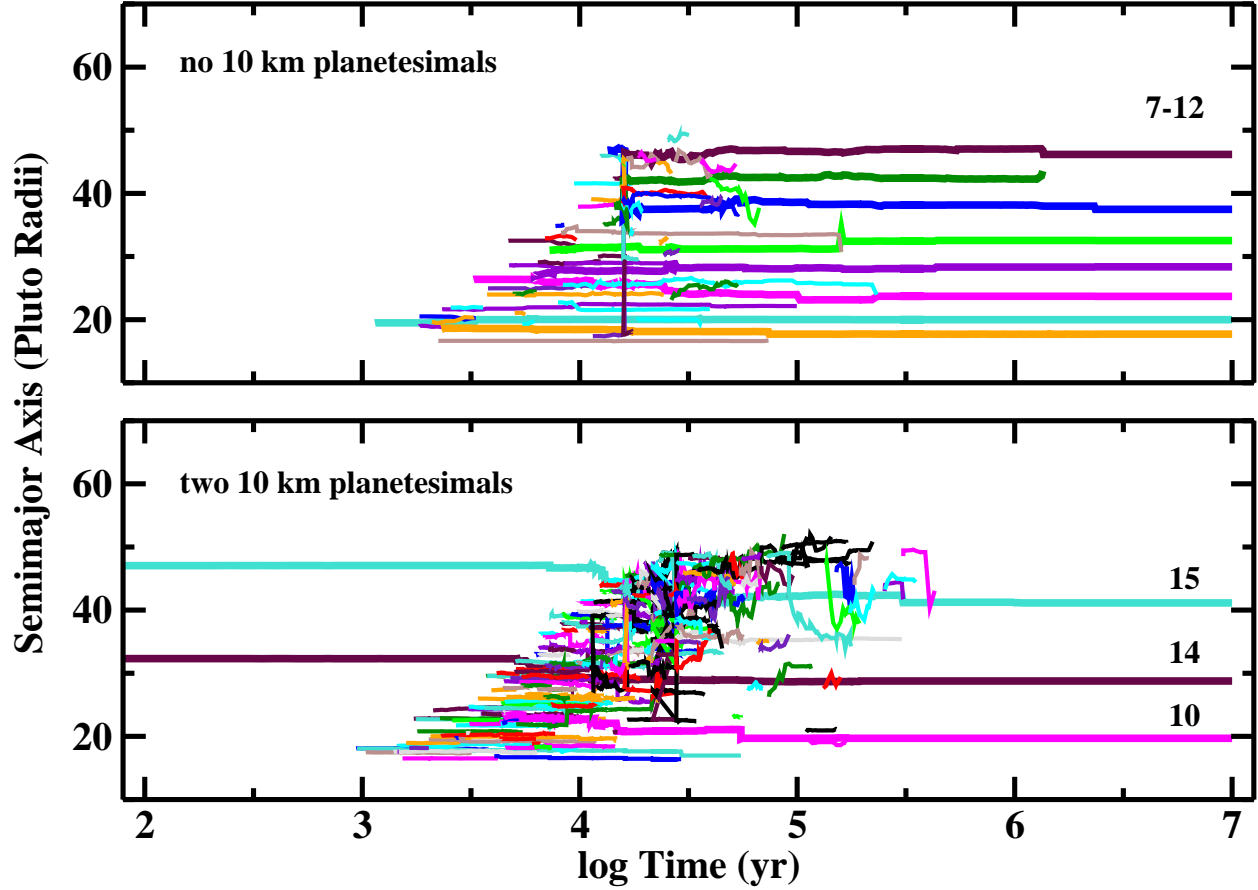


Fig. 8.— As in Fig. 7 for an initial disk mass  $m_d \approx 3 \times 10^{19}$  g composed of 0.1 km and smaller planetesimals. Upper panel: evolution without larger planetesimals; lower panel: evolution with two 10 km planetesimals. Calculations with a several initial large planetesimals yield fewer, larger satellites than calculations without large planetesimals.

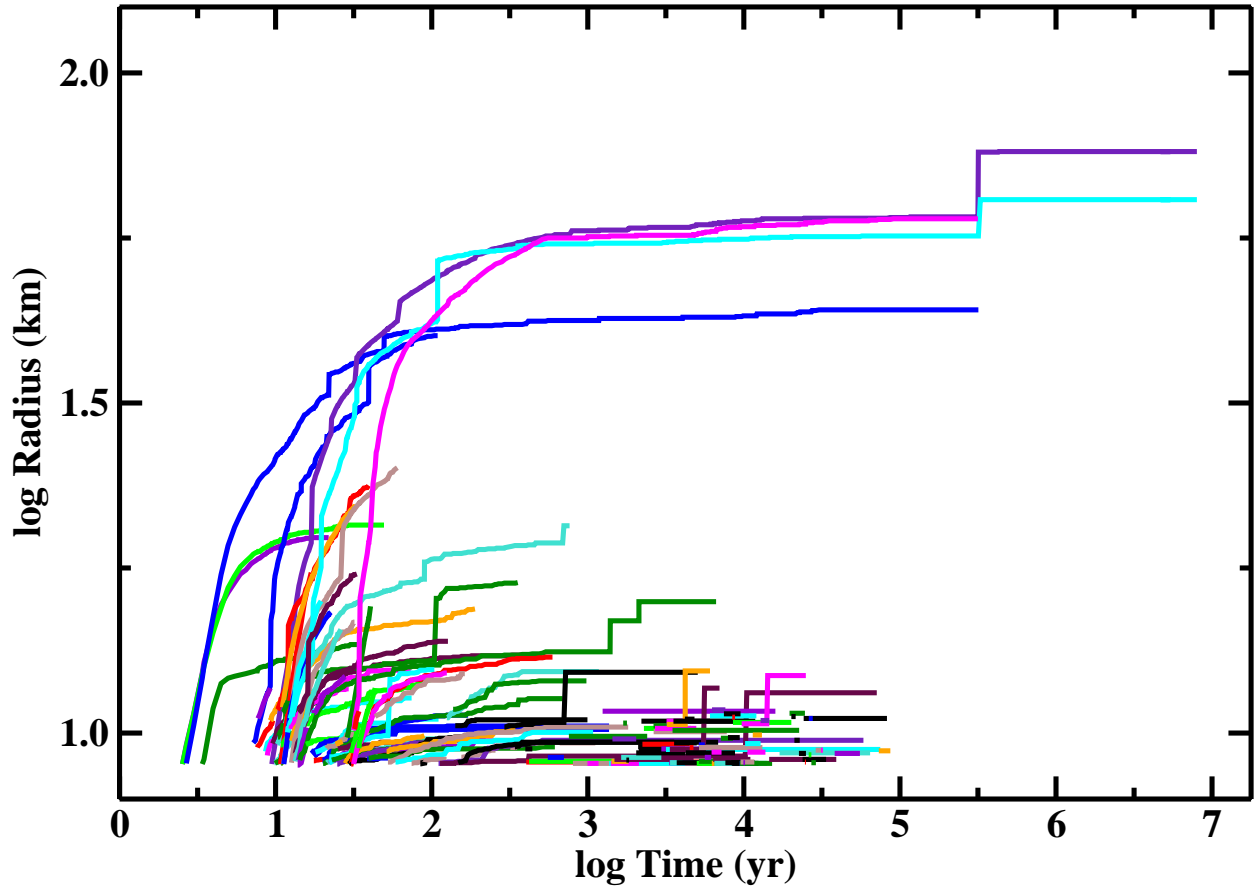


Fig. 9.— Radius evolution for  $n$ -bodies. The calculation begins with  $m_d = 3 \times 10^{21}$  g and  $m_{pro} = 3 \times 10^{18}$  g. Once a few large objects form, they gradually accrete all of the smaller  $n$ -bodies.

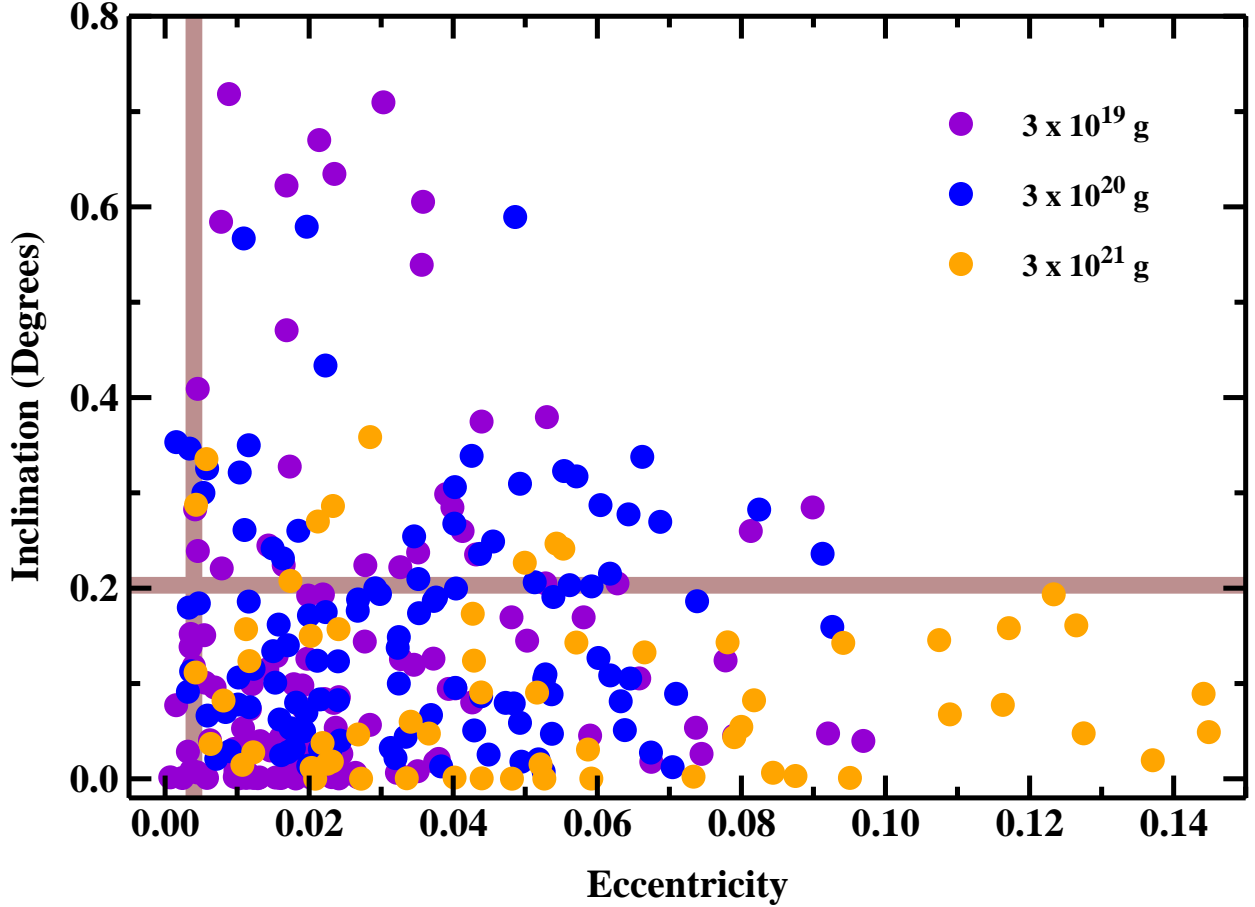


Fig. 10.— Distribution of orbital eccentricity  $e$  and inclination  $i$  for satellites produced in disks with initial masses of  $3 \times 10^{19}$  g (violet points),  $3 \times 10^{20}$  g (blue points), and  $3 \times 10^{21}$  g (orange points). Although there is no clear correlation of average orbital inclination with disk mass, disks with larger initial masses produce satellites with larger average  $e$ . The horizontal and vertical bars indicate the average of the measured eccentricity and inclination for Nix ( $e_N$  and  $i_N$ ) and Hydra ( $e_H$  and  $i_H$ ) from the 2007 Jacobson PLU017 JPL satellite ephemeris. For the model satellites, 10% have  $e \lesssim e_{H,N}$  and 83% have  $i \lesssim i_{H,N}$ .

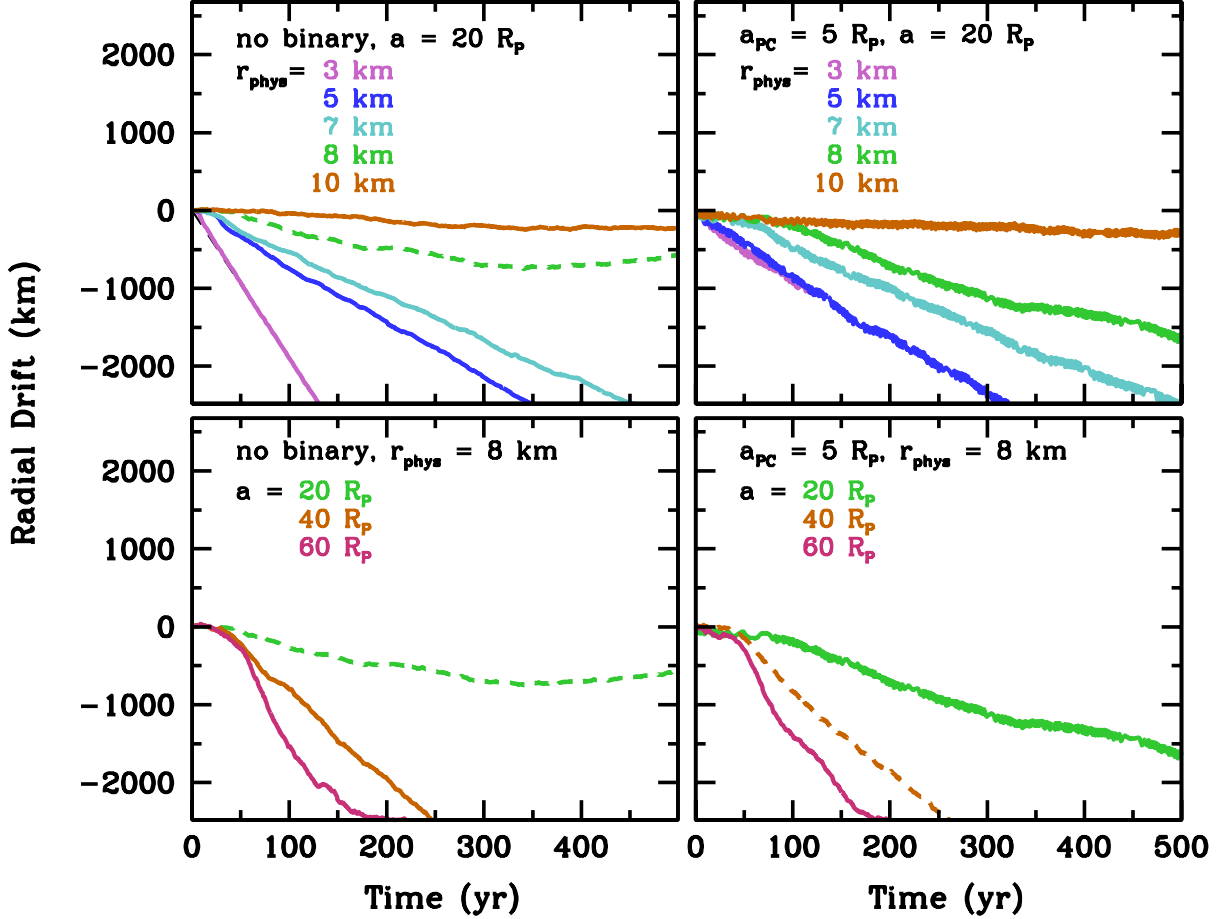


Fig. 11.— Migration of single satellites through a particle disk. Each trace shows the result of a simulation with either a single central point mass (left panels, with mass equal to the sum of  $M_P$  and  $M_C$ ) or a central Pluto-Charon binary with orbital separation of  $5R_P$ . The legends give the physical radii of each satellite with  $\rho = 1 \text{ g/cm}^3$ ; the legends also show the semimajor axis of the satellites’ initial orbit. The disk model has a total mass of  $3 \times 10^{20} \text{ g}$  in a disk with surface density  $\Sigma \sim 1/a$  extending in radius from  $20R_P$  to  $70R_P$ . Note that migration is more commonly in the inward direction, however, it can be outward by chance. Solid curves show inward drift, while dashed lines refer to outward motion.

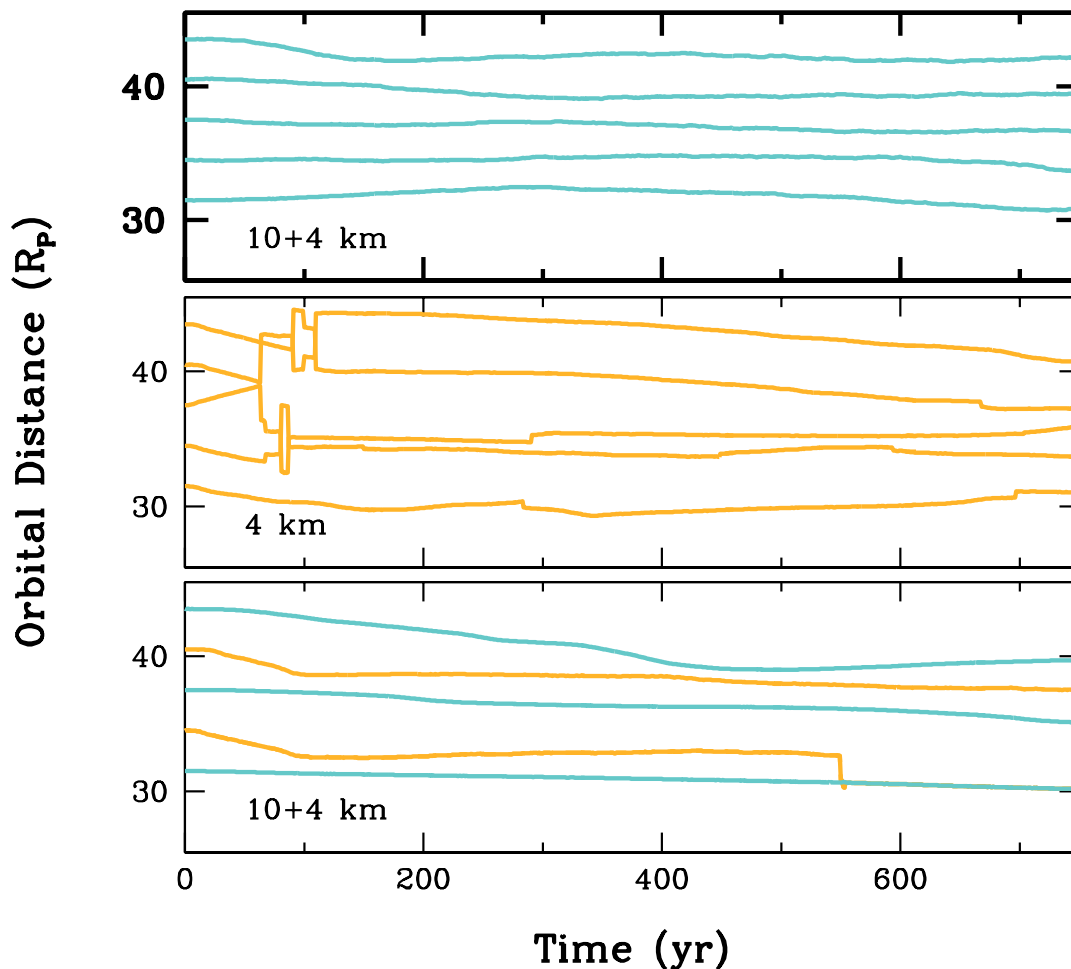


Fig. 12.— Migration of multiple satellites around a tight Pluto-Charon binary. The binary orbit and disk model are the same as in Figure 11, except that each set of five satellites is embedded in a  $20R_P$  annulus of disk particles. Each panel gives an example of the simulation output; the upper panel shows equal-mass 10 km satellites, while the middle panel tracks smaller 4 km bodies. In the former case, some radial drift occurs but does not lead to significant scattering or merging. The smaller satellites are more interactive; the middle panel shows an orbit crossing event. The lower panel illustrates differential migration in which a smaller body merges with a larger one.

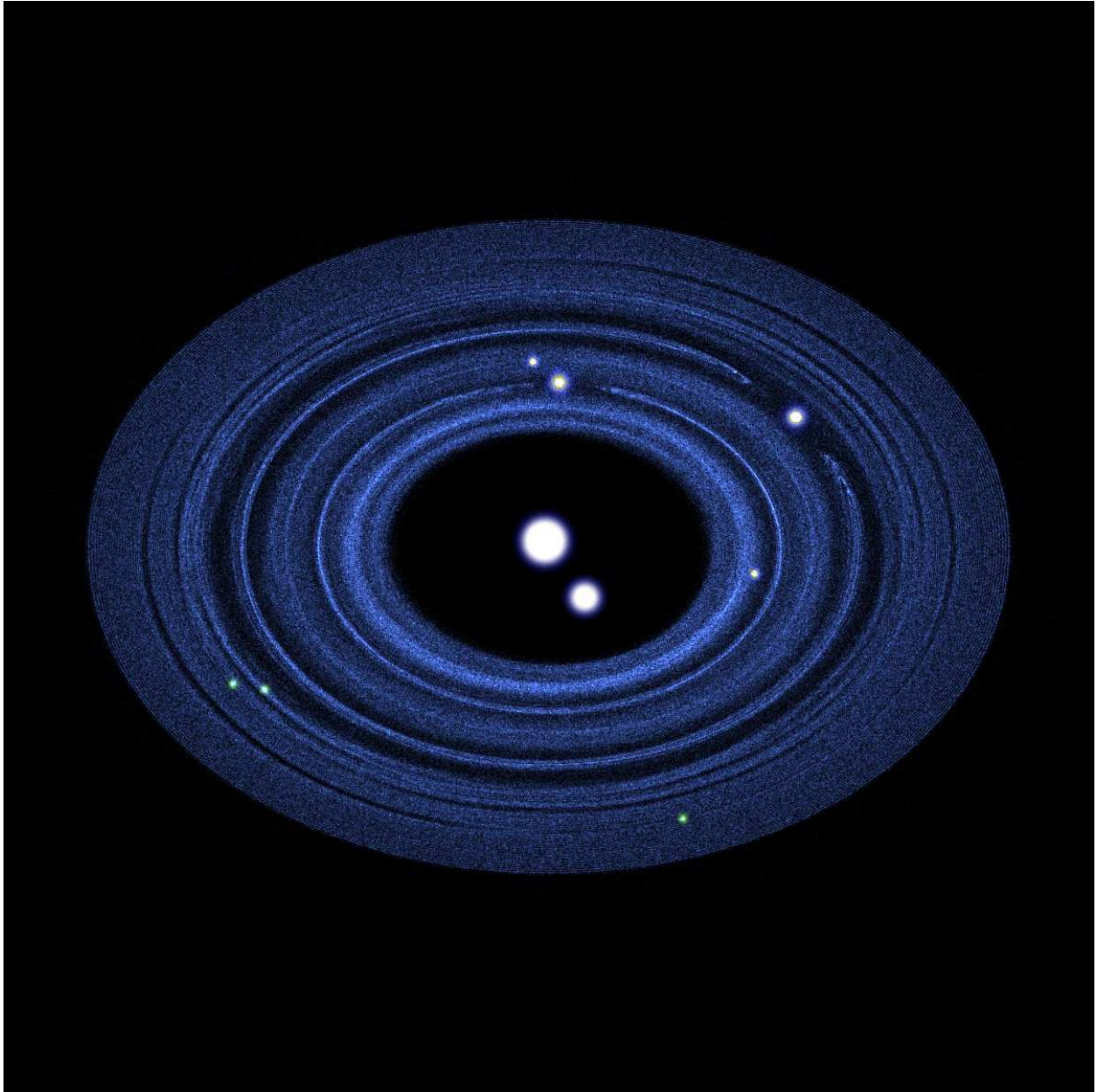


Fig. 13.— Predicted system configuration for the Pluto–Charon system. The Pluto–Charon binary (represented by the two largest white disks), the four small satellites – P5, Nix, P4, and Hydra (represented by the four small white disks), and three smaller satellites (represented by the green disks) lie within an extended ensemble of solid particles shown as small blue dots. This configuration is the result after twenty years of a computer simulation with two million massless tracer particles surrounding the known and predicted moons. On this short time scale, the small satellites clear out most of the tracers along their orbits. On much longer time scales, satellites will clear tracers from a larger fraction of their orbits.